Digital Beamforming for Spaceborne Reflector SAR Systems via FIR Filter Networks in the Presence of Uncertainties

Koen Mouthaan

September 2017

Declaration of Authorship

I hereby certify that this thesis has been composed by me and is based on my own work, unless stated otherwise. No other person's work has been used without due acknowledgement in this thesis. All references and verbatim extracts have been quoted, and all sources of information, including graphs and data sets, have been specifically acknowledged. This thesis has not been submitted for any degree in any university previously.

Place and date	Singapore, 15 September 2017
Signature	Koen Mouthaan[1]

[1] Signed version available on request.

Abstract

Tandem-L is a proposed fully polarimetric bistatic spaceborne Synthetic Aperture Radar (SAR) mission. The aim of the mission is to monitor dynamic processes on the Earth's surface. The proposed radar satellite employs an array-fed reflector antenna with a digital feed-array for high sensitivity, high-resolution wide-swath SAR. With digital beamforming (DBF) multiple radar echoes can be tracked simultaneously on ground with high gain. In DBF, a priori information about the antenna patterns of the antenna is used. However, actual antenna patterns may vary due to deformations of the reflector resulting from, for example, in-orbit thermal effects. In this thesis, the impact of reflector deformations on antenna parameters in elevation and DBF performance in elevation is presented and discussed. Additionally, the impact of the frequency dependent behavior of the antenna on DBF parameters is presented. The thesis concludes with recommendations for further research.

Acknowledgements

I thank the following people at the Microwaves and Radar Institute of the German Aerospace Center (DLR), Oberpfaffenhofen, Germany.
First and foremost, I thank Dr.-Ing. Sigurd Huber, my supervisor in the project, for his continuous support and the good discussions on reflector antennas and digital beamforming for space missions.
I also thank Dr.-Ing. Gerhard Krieger for enabling and supporting the project. And I thank Dr.-Ing. Marwan Younis and Prof. Dr.-Ing. Alberto Moreira for their support.
Finally, I thank Prof. Dr.-Ing. Klaus Brieß and Dipl.-Ing. Cem Avsar of the Technical University of Berlin for their continuous support.

Contents

Acronyms and Symbols

Acronyms

acronym	description
ADC	analog-to-digital converter
DBF	digital beamforming
EM	electromagnetic
FFT	fast Fourier transform
FIR	finite impulse response
IF	intermediate frequency
LEO	low Earth orbit
LO	local oscillator
MVDR	minimum variance distortionless response
PO	physical optics
PT	point target
RF	radio frequency
Radar	radio detection and ranging
RCS	radar cross section
RX	receive
SCORE	scan-on-receive
TRM	transmit/receive module
TX	transmit

Lower Case Symbols

symbol	unit	description
$a_{\mathrm{RX},i}$	-	complex-valued antenna far field pattern belonging to an individual element/channel in direction of point target
f	Hz	frequency
f_c	Hz	center frequency
f_S	Hz	temporal sampling frequency
h_s	m	orbit height
i	-	count variable for channels
m	-	count variable for FIR filter subbands
n	-	count variable for array elements
n	-	discrete time variable
o	-	backscatter/reflectivity function
p	$\sqrt{\mathrm{W}}$	transmitted waveform
$\boldsymbol{r}$	m	spatial coordinate in Euclidian space
$\boldsymbol{r_s}$	m	position vector of the SAR sensor
t	s	continuous time variable
u	$\sqrt{\mathrm{W}}$	SAR raw data signal
u_BB	$\sqrt{\mathrm{W}}$	baseband signal
w	-	complex weight/excitation coefficient
$\boldsymbol{w}$	-	complex weight vector

Capital Symbols

symbol	unit	description
A	m	amplitude of deformation
B	Hz	signal bandwidth
F	m	focal length
$HPBW$	rad	half power beamwidth
M	-	number of FIR filter subbands
N_c	-	number of channels
N_coef		number of FIR filter coefficients
N_x	-	number of feed elements in elevation
N_y	-	number of feed elements in azimuth
N_ρ	-	number of quarter period deformations w.r.t. radius ρ
N_ϕ	-	number of half period deformations w.r.t. angle φ
PRF	Hz	pulse repetition frequency
PRI	s	pulse repetition interval
$PSLR$	-	peak-sidelobe ratio
SNR	-	signal-to-noise ratio

Greek Symbols

symbol	unit	description
θ_{bore}	rad	boresight angle with respect to nadir
θ_{l}	rad	look angle with respect to nadir
ρ	m	radius
ρ_c	m	radius of a circle
τ	s	delay time
τ_p	s	pulse duration
φ	rad	angle

Constants and numbers

symbol	value	unit	description
c	299792458	ms^{-1}	speed of light in free space
j	$\sqrt{-1}$	-	imaginary number
π	3.141592	-	mathematical constant
r_e	6378137	m	WGS84 Earth radius at equator

Chapter 1

Introduction

Tandem-L is a proposed fully polarimetric bistatic spaceborne Synthetic Aperture Radar (SAR) mission. The aim of Tandem-L is to monitor dynamic processes on the Earth's surface [1], [2]. Several major challenges are associated with the various fields of applications of Tandem-L [3]. To help address these challenges, the proposed radar satellite employs an array-fed reflector antenna with a digital feed array for high sensitivity, high-resolution, wide-swath SAR. With digital beamforming (DBF), radar echoes can be tracked on ground with high gain using the concept of scan-on-receive (SCORE). In DBF a priori information about the antenna patterns of the antenna is required. However, actual antenna patterns may vary due to deformations of the reflector resulting from, for example, in-orbit thermal and mechanical effects. The change in antenna behavior will impact DBF performance and SAR imaging performance.

1.1 Research questions

The following two research questions are addressed in this thesis.

1. What is the impact of deformations in the parabolic reflector on antenna performance and DBF performance in elevation?

2. What is the impact of the frequency dependent antenna behavior on the antenna parameters and on DBF performance?

Furlable reflector antennas are exposed to thermal and mechanical forces during fabrication, launch, deployment, and use. For example, in orbit the antenna is exposed to the heating and cooling cycles of sun and darkness in the sunlit and eclipse phase, respectively. These forces can deform the surface of the reflector either temporarily or permanently. Deformations, in turn, will impact the performance of the antenna. In this thesis the impact of antenna deformations on the antenna parameters and DBF performance in elevation is investigated. A linear FM chirped pulse is transmitted. Because the antenna parameters of the array-fed reflector antenna are frequency dependent, DBF will also be impacted. Either DBF at a single frequency, such as the center frequency, is applied, and deterioration in DBF

is accepted. Or frequency adaptive DBF is used to improve DBF, at the expense of increased computational complexity. Therefore, to address these questions, this thesis first considers the impact of these frequency dependencies when applying DBF based on the center frequency. Subsequently, frequency adaptive DBF is applied and compared with the case without frequency adaptation.

1.2 Scope of work

To assess the impact of reflector deformations and frequency dependencies in the antenna on DBF performance, a computational model is built in IDL [4]. This model incorporates SCORE beamforming in elevation to track the return of a single pulse scattered by a point. The underlying hypothesis is that a scene is considered as a superposition of infinite many point targets. Beamforming in azimuth and full SAR imaging can be added later in a subsequent project. The minimum variance distortionless response (MVDR) technique is used for beamforming, with a further simplification in relation to the required noise covariance matrix. Investigation of other techniques can be undertaken in a subsequent project. The model allows for M simultaneous digital beams, each tracking a distinct part of the pulse. Related to the multibeam operation, the model also incorporates FIR filters to filter parts of the pulse associated with each beam. In each FIR filter the number of coefficients N_{coef} is a parameter. One aim of this project is to investigate the simultaneous influence of the number of digital beams M and number of FIR coefficients N_{coef} on DBF performance. On the one hand, it is expected that increasing M and N_{coef} will improve DBF performance. On the other hand, this will increase computational burden significantly. Therefore, an assessment must be made of the typically required values for these two parameters.

The model is first applied to a point scatterer at boresight, without any deformation in the reflector. The results serve as the baseline for the remainder of the thesis. Most of the operational parameters for this baseline case are representative for Tandem-L. Subsequently, the model is applied to several cases of reflector deformations and the impact on antenna performance and DBF performance is compared with the baseline case. Finally, the impact of frequency dependencies of the antenna on the antenna parameters and DBF performance is investigated.

1.3 Outline

This thesis is organized as follows. In chapter 2 the computational model for digital beamforming in elevation is discussed. The computational model is then applied to the case of beamforming without deformation in the reflector to a point target (PT) at boresight in chapter 3. This case serves as the baseline for comparison with the cases in the subsequent chapters. In chapter 4 the impact of deformations in the reflector on antenna parameters and digital beamforming parameters is investigated. Chapter 5 discusses the impact of the frequency dependent behavior of the antenna

on the antenna performance and the DBF parameters. This thesis concludes with a set of conclusions and recommendations in chapter 6.

Chapter 2

Computational model

This chapter introduces the model underlying the results of the following two chapters. The aim of this chapter is not to provide complete and thorough detail of the model. Instead, the aim is to provide a concise introduction to some of the key techniques employed in the digital beamforming. This chapter is based on the work by Huber [5] to a significant extent, and the interested reader is referred to that work and the references therein.

The starting point of the description is the SAR instrument using an array-fed reflector antenna in section 2.1. Subsequently, wave propagation of the EM pulse from SAR instrument to Earth is described in section 2.2, followed by the generic equation for the signal received by the array elements and the baseband signal of each channel in section 2.3. In section 2.4, SCORE DBF is discussed as well as the associated look angle. In this thesis, minimum variance distortionless response (MVDR) DBF is used to form the digital beams tracking the pulse, as discussed in section 2.5. Instead of DBF with a single beam, this thesis uses multiple beams, in which each beam tracks a separate part of the pulse, as described in section 2.6. To facilitate DBF with multiple beams, FIR filters are used to separate out the single pulsed chirp into subbands, as discussed in section 2.7. Each subband is then associated with a beam. To analyze the signal-to-noise ratio of the digital beamformer, noise is incorporated into the model using the random generator available in IDL, as discussed in section 2.8. All operations performed on the sampled baseband signal are also performed on the noise data. That is, at the output of the beamformer the signal and the noise are available separately, which are then used to compute the signal-to-noise ratio. Lastly, in section 2.9 the GRASP simulations are briefly introduced, as well as the antenna parameters that are exported from GRASP into the computational model.

2.1 SAR instrument

The SAR instrument uses an array-fed reflector antenna combined with sampling of all individual channels. The feed array consists of an rectangular array of $N_c = N_x \cdot N_y$ channels, with N_x the elements in elevation and N_y the elements in azimuth.

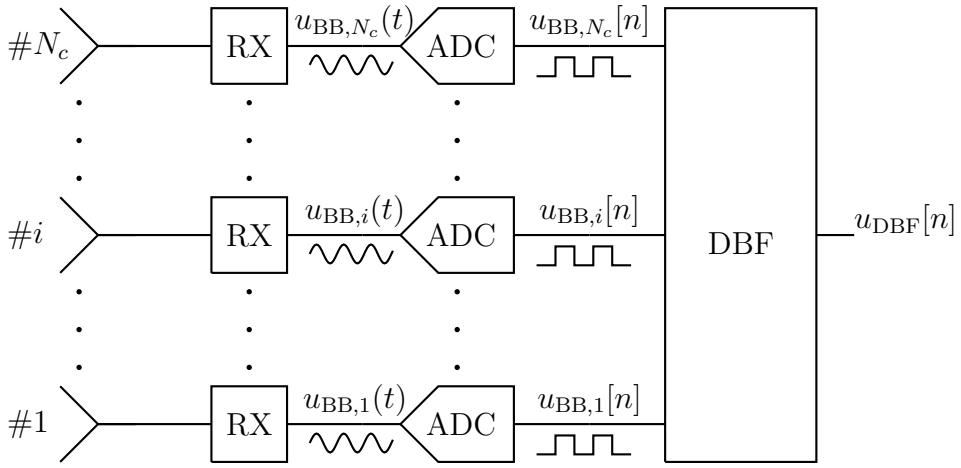

Figure 2.1: Receiver architecture with N_c channels.

In transmit mode all channels are activated to transmit a pulse with duration τ_p. In receive mode, each of the N_c channels is connected to a receiver/down-converter, followed by an analog-to-digital converter (ADC). The receive mode is schematically shown in Fig. 2.1. In this figure the N_c channels are shown on the left. Each signal goes to a receiver (RX) where the RF signal is down-converted in quadrature to a complex baseband signal $u_{\mathrm{BB},i}(t)$. The baseband signal $u_{\mathrm{BB},i}(t)$ is then sampled at a rate f_{s} into the sampled baseband signal $u_{\mathrm{BB},i}[n]$. The key point to note is that N_c digital streams are available for DBF processing, indicated by the DBF block in the figure.

Throughout this thesis, time is the independent variable, and all signals and several parameters are computed as function of time. Time t = 0 denotes the moment the front edge of the transmitted pulse leaves the SAR instrument. In the computations, a uniformly sampled time-array is established using a sampling frequency f_{s}. Then all signals are computed for all discrete times. Practically speaking, only time intervals of interest are computed, i.e., sampling starts slightly before the first scattered signal would reach the SAR instrument.

2.2 Wave propagation

Before considering digital beamforming, it is important to understand how the pulse travels along the surface of the Earth as a function of time. Consider a satellite at an orbit height h_s of 750 km above Earth, transmitting an electromagnetic (EM) pulse of $\tau_p = 500$ μs. The spatial "length" of the pulse is 150 km ($c{\cdot}\tau_p$). Isotropic radiation, originating at the SAR instrument, and spherical wave propagation is assumed. In Fig. 2.2 the EM pulse is shown for various time instances.

At t = 2.5 ms the front of the pulse reaches Earth, and at t = 3.0 ms the end of the pulse reaches Earth. Subsequently, the wave propagates further. The key point

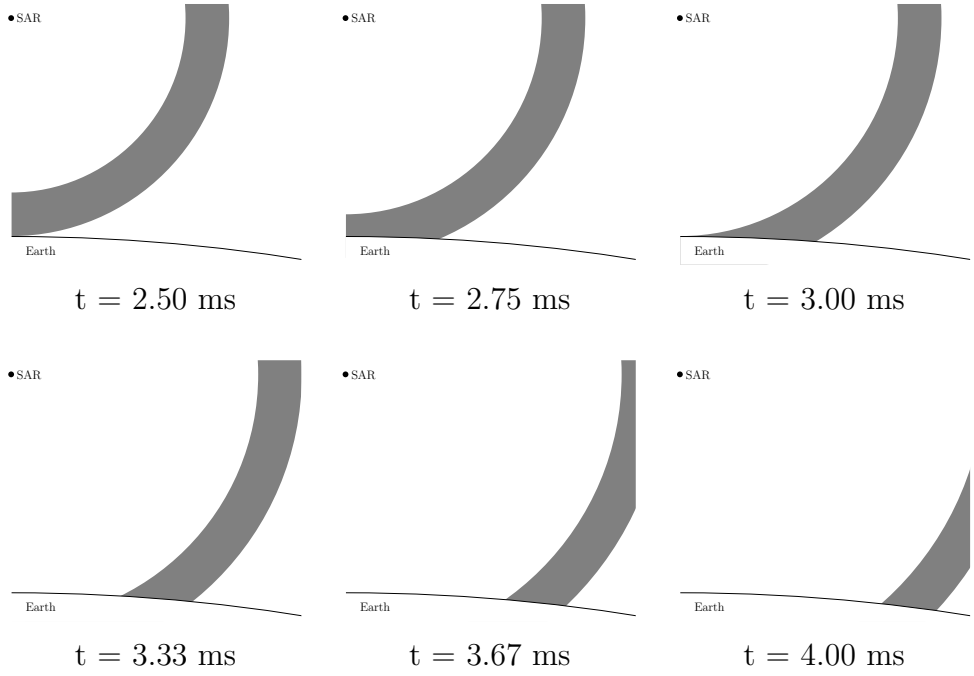

Figure 2.2: Electromagnetic pulse propagation from SAR on satellite to Earth for various time instances.

to note now is that the front of the wave does not travel with constant speed along the surface of Earth. The location of the front of the pulse, or any other part of the pulse, for any given time is found easily by computing the intersection of two circles; the first circle, with constant radius r_e, represents Earth, and the second circle, with the radius expanding with the speed of light ($c{\cdot}t$), represents wave propagation.

2.3 Baseband signal

In section 4.1 in [5] the multi-channel expansion of the received signal is provided (eqns. (4-2)-(4.4)). Here, an expression for the baseband signal is derived by reducing these equations as follows. The transmitted waveform is a pulse with a linear frequency chirp. The pulse duration is denoted by τ_p, and the bandwidth of the chirp by B:

$$p(t) = \text{rect}\left(\frac{t - \tau_p/2}{\tau_p}\right) e^{j\pi(B/\tau_p)(t-\tau_p/2)^2} \tag{2.1}$$

The waveform is up-converted to a microwave signal with center frequency f_c, amplified by a power amplifier, and radiated by the antenna. The EM wave propagates through free space, reflects on a point target, propagates back to the antenna, and is received there by each of the array feeds of the reflector antenna, and then finally down-converted to a baseband signal. Assuming that the delay from point scatterer to each of the feeds is the same τ, the expression for the received baseband signal

is:

$$u_{\mathrm{BB},i}(t) = p(t-\tau)a_{\mathrm{RX},i} \tag{2.2}$$

where the gain of the i-th feed-element in the direction of the point target is denoted by $a_{\mathrm{RX},i}$. Note that, under the narrowband assumption, delays are encoded in the phase of each of the far field patterns $a_{\mathrm{RX},i}$. The influence of power amplification, radiation by the antenna, propagation through free space, and reflection on the point target, on the amplitude and phase of the baseband signal has been removed from the expression, because they are assumed to be the same for all feed elements. The baseband signal $u_{\mathrm{BB},i}(t)$ is sampled with the selected sample frequency f_{s} to obtain the digitized baseband signal $u_{\mathrm{BB},i}[n]$.

2.4 Single beam SCORE and look angle

The N_c data streams of sampled received signals, shown in Fig. 2.1, allow digital beamforming in which a single beam tracks the pulse propagating along Earth's surface using SCORE. This technique is illustrated in Fig. 2.3. In the figure the

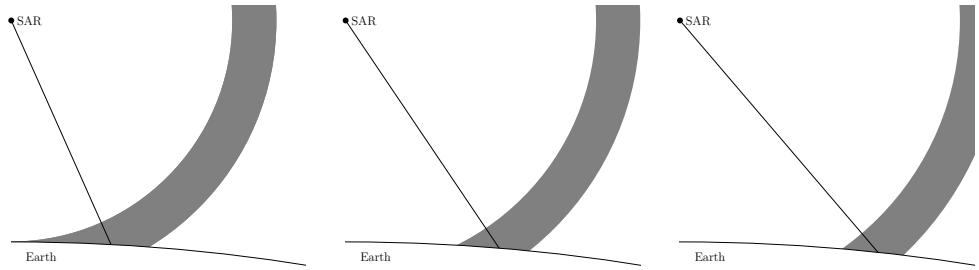

$\theta_{\mathrm{l}} = 27°$ $\theta_{\mathrm{l}} = 34°$ $\theta_{\mathrm{l}} = 40.5°$

Figure 2.3: SCORE digital beamforming with a single beam tracking the pulse.

EM pulse propagation is shown, as well as the progression of the digital beam and associated look angles θ_{l} for tracking the center of the pulse. Fig. 2.4 shows the implementation of the DBF block, shown on the right in Fig. 2.1, enabling SCORE with a single beam.

The weights w_i are computed such that a digital beam is formed which tracks the pulse traveling over ground. To compute these weights, first the look angle with respect to nadir must be known for a SCORE beamformer with one beam. Consider the example again of a SAR instrument at an orbit height $h_s = 750$ km, transmitting a pulse with $\tau_p = 500$ μs. In Fig. 2.5 the look angle w.r.t. nadir for the front of the pulse and the end of the pulse is shown. At t = 2.5 ms the front of the EM wave reaches Earth and a backscattered signal would reach the receiver at t = 5 ms. Therefore, at t = 5 ms the look angle starts at 0° and then increases with time according to the discussion above. Similarly, the end of the pulse is 0.5 ms after the front of the pulse. The associated look angle is a 0.5 ms delayed version of the look

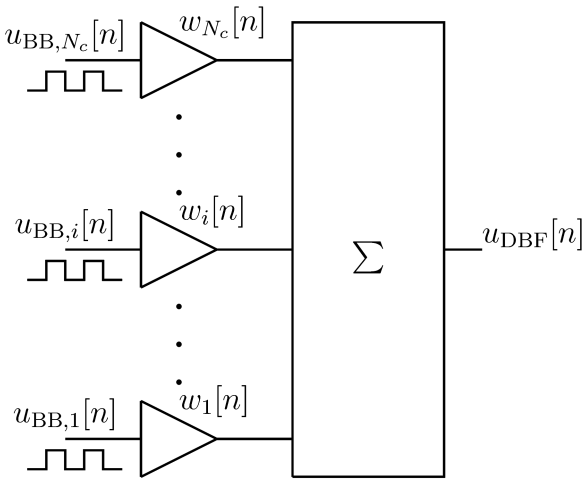

Figure 2.4: Implementation of SCORE DBF with a single beam tracking the pulse.

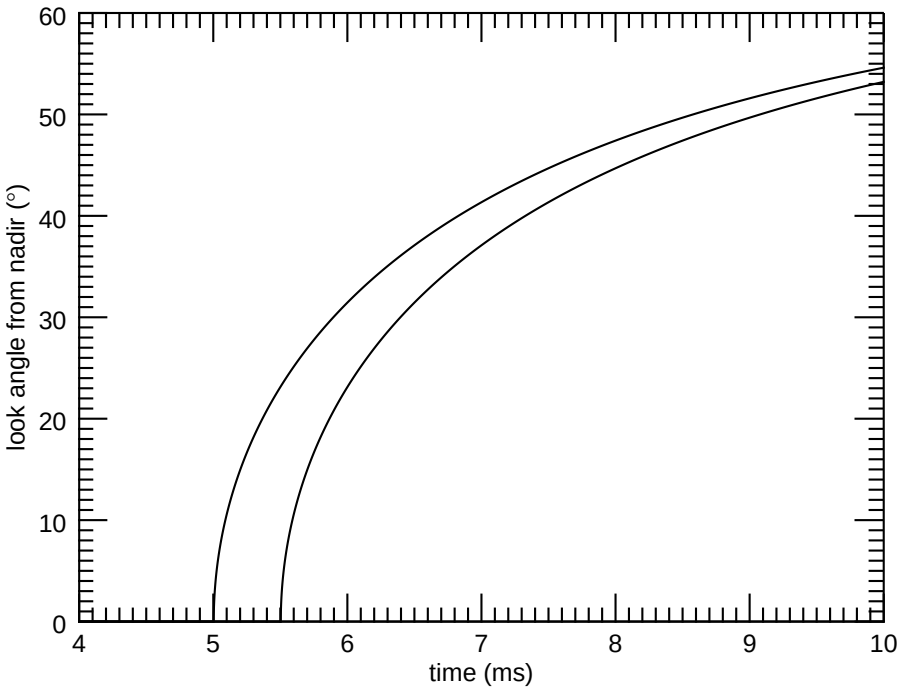

Figure 2.5: Look angles w.r.t. nadir for the front and the end of the pulse. The SAR is at an orbit height $h_s = 750$ km, transmitting a pulse with $\tau_p = 500$ μs.

angle for the front of the pulse. In case the center of the pulse must be tracked, the look angle curve for the front of the pulse must be delayed by 0.25 ms. It is noted that typical look angles for Tandem-L lie between 23° and 41°.

2.5 MVDR beamforming

Different DBF algorithms can be used. In [5], unity beamforming, minimum variance distortionless response (MVDR) beamforming, and linear constraint minimum variance (LCMV) beamforming are considered. In the remainder of this thesis, MVDR beamforming is used. Here, equation (4.53) of section 4.3.3. in [5] is used. In principle, MVDR requires the noise covariance matrix or an estimator of this matrix. For reason of simplicity and in the absence of good knowledge of the noise processes in the actual receiver, the noise covariance matrix is assumed equal to the identity matrix multiplied by the noise variance.

Note that, in relation to SCORE with a single beam, the beamforming weights must be computed for every instance of the sampled time, because the digital beams track the pulse over Earth's surface. Obviously, in case multiple beams are used, the weights must be computed for each time instance and for each beam.

Computationally, the following challenge may occur. The GRASP simulations of the array-fed reflector array result in the antenna parameters for a set of discrete elevation angles. SCORE beamforming usually requires elevation angles that are in between these discrete elevation angles. And, therefore, accurate interpolation of the GRASP antenna parameters is needed to obtain radiation patterns at the required SCORE elevation angles. This may increase the computational burden significantly, because, in case of beamforming in elevation with N_x channels, the interpolation must be performed for all N_x channels for each discrete time point and for each digital beam. Note that in the implementation in an actual system, the weights are pre-computed and stored in the system, i.e., the above challenge applies to simulations discussed in this thesis.

2.6 Multi beam SCORE and look angles

In section 2.4, SCORE with a single beam is considered. It can be advantageous to use multiple digital beams, in which each beam tracks a particular and distinct part of the pulse. For example, consider a linear chirped pulse with a bandwidth $B = 100$ MHz and pulse duration $\tau_p = 500$ μs. One beam tracks the center of the first half of the pulse, and a second beam tracks the center of the second half of the pulse. This technique is illustrated in Fig. 2.6. Again, the EM pulse propagation is shown, as well as the progression of the two digital beams and their associated look angles $\theta_{\mathrm{l},1}$ and $\theta_{\mathrm{l},2}$ for tracking the pulse. Note that the difference between the two look angles $\theta_{\mathrm{l},1}$ and $\theta_{\mathrm{l},2}$ reduces as the pulse propagates further. The beamformer supporting this operation is shown in Fig. 2.7. In this figure, each of the N_c baseband data streams is first split into two, resulting in $2N_c$ data streams. The first set of N_c data streams is used to track the first half of the pulse, and the second set is used to track the second half of the pulse. Because the pulse is a linear frequency chirp, the first set of data streams is passed through a bandpass filter with 50 MHz bandwidth and a center frequency of -25 MHz (w.r.t. the center frequency). And the second set of data streams is passed through a bandpass filter with 50 MHz

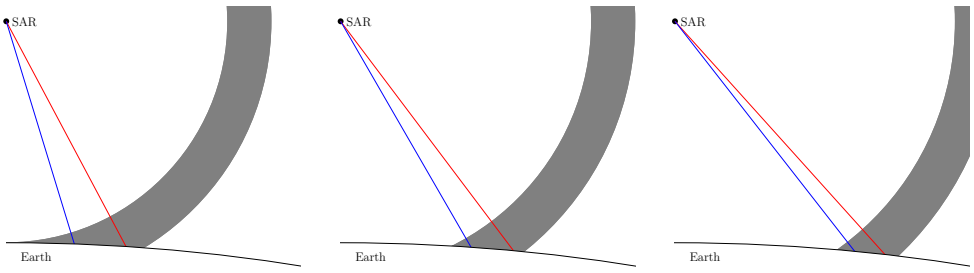

$\theta_{l,1} = 28°$ $\theta_{l,2} = 17°$ | $\theta_{l,1} = 37°$ $\theta_{l,2} = 30°$ | $\theta_{l,1} = 42°$ $\theta_{l,2} = 38°$

Figure 2.6: SCORE DBF with two beams tracking the pulse.

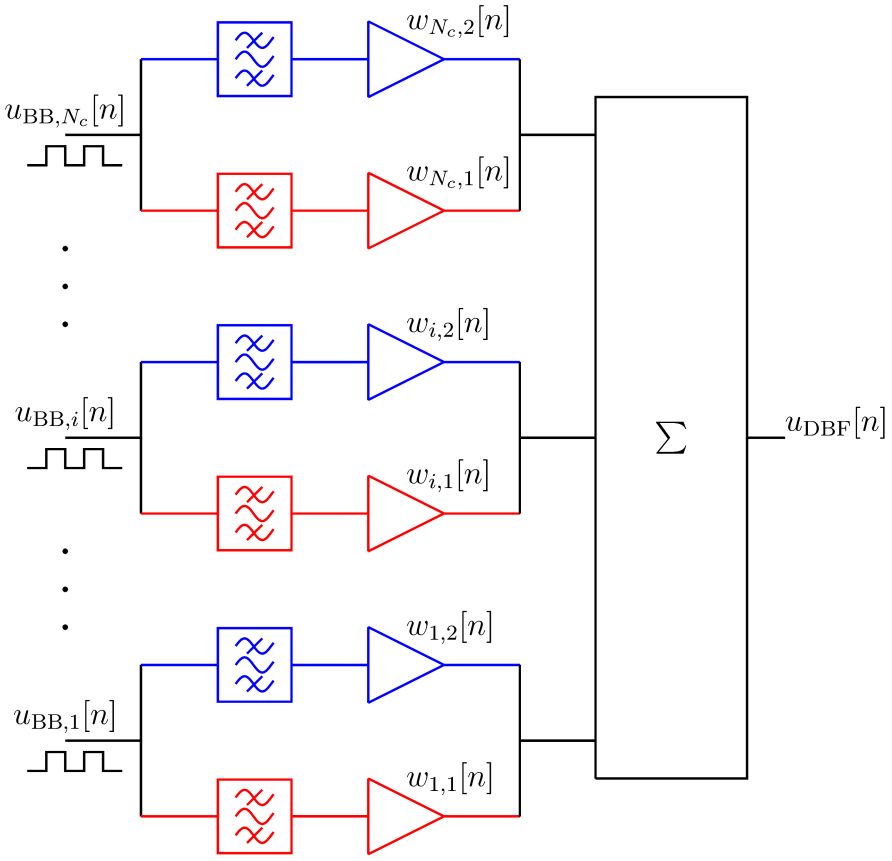

Figure 2.7: Implementation of SCORE DBF with two beams tracking the pulse.

bandwidth and a center frequency of 25 MHz. Each of the signals in the first set is then multiplied with the digital beamforming coefficients $w_{i,1}$ for tracking the center of the first half of the pulse. And each of the signals in the second set is then multiplied with the DBF coefficients $w_{i,2}$ for tracking the center of the second half of the pulse. Obviously, this concept can be easily expanded to include a larger number of beams. Therefore, the number of beams and associated subbands M becomes a

parameter in DBF. Roughly speaking, increasing the number of subbands M will improve reconstitution of the original pulse. However, computational effort increases linearly with the number of subbands, which is a severe penalty. Note, again, that this penalty applies to the simulations discussed here.

When more than a single beam is used, the associated look angles for each subband must be computed. As an example, consider the case in which the pulse of $\tau_p = 500$ μs is divided into $M = 5$ subbands of equal duration of 100 μs. The look angle tracks the center of each subband, not the edges. In Fig. 2.8 the look angle for the five subbands is shown as function of time.

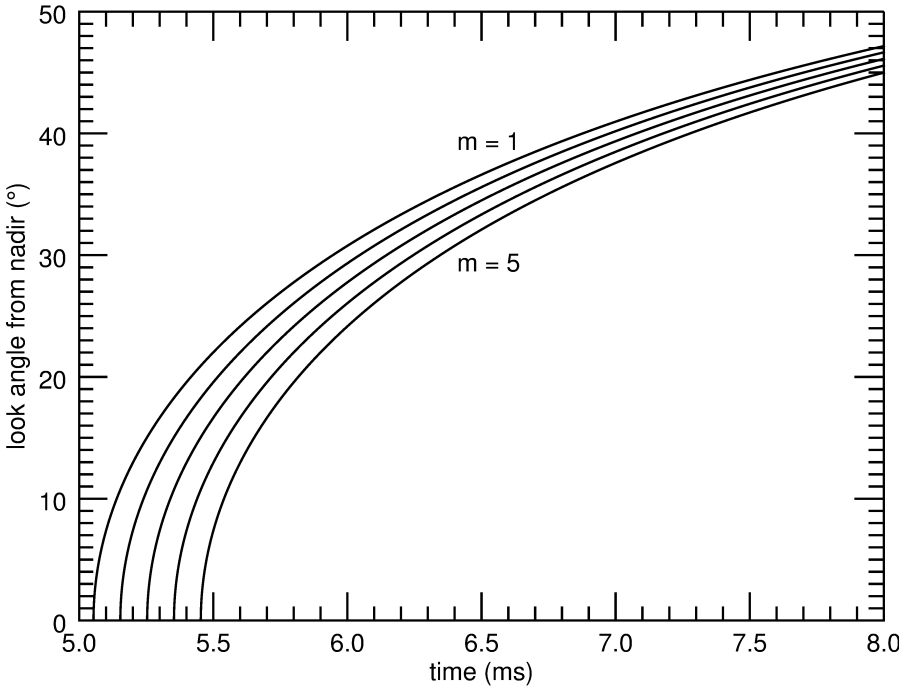

Figure 2.8: Look angles w.r.t. nadir for five subbands (orbit height of SAR instrument $h_s = 750$ km, and transmit pulse $\tau_p = 500$ μs).

2.7 FIR filtering

The previous section discusses SCORE with multiple beams. This approach requires digital filtering of the subbands. A variety of suitable digital filters is available, such as recursive filters and FIR filters. In this thesis FIR filters are used, for their ease of implementation, robustness, and stability. The interested reader is referred to section 4.4.1 in [5], and the implementation equations (4.79)-(4.81) contained therein. It is important to note that FIR filtering introduces an additional parameter in the digital beamforming: the number of FIR filter coefficients N_{coef}.

As an example, a linear chirp with bandwidth $B = 100$ MHz and pulse duration $\tau_p = 100$ μs is considered. The FIR filter response for $M = 2$, 5, and 10 subbands are shown in Fig. 2.9, with the number of coefficients being varied from $N_{\text{coef}} =$ 11, 21, and 51. The figures also show the summation of the subbands, i.e., the reconstructed pulse.

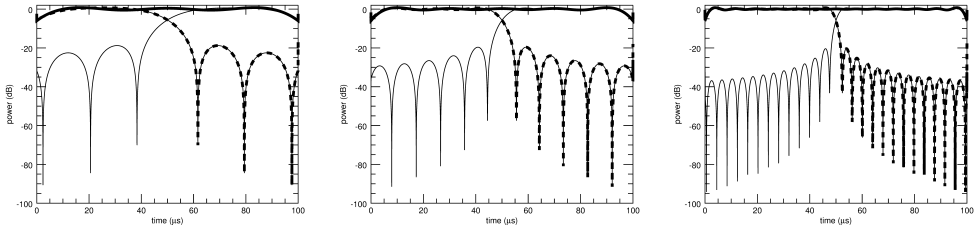

$M = 2$, $N_{\text{coef}} = 11$ $M = 2$, $N_{\text{coef}} = 21$ $M = 2$, $N_{\text{coef}} = 51$

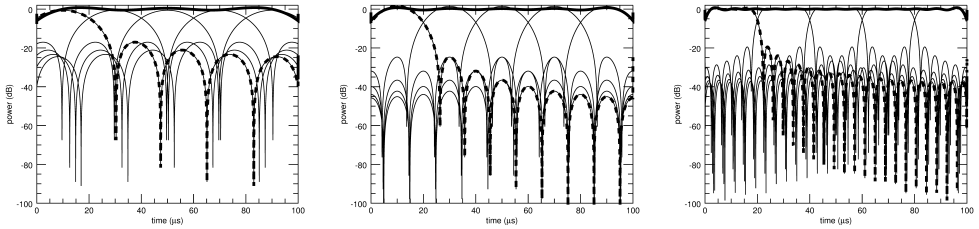

$M = 5$, $N_{\text{coef}} = 11$ $M = 5$, $N_{\text{coef}} = 21$ $M = 5$, $N_{\text{coef}} = 51$

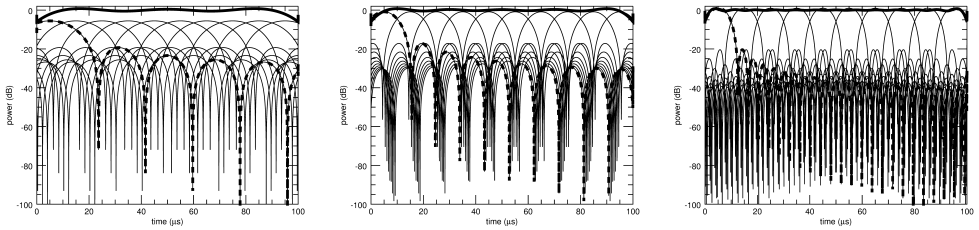

$M = 10$, $N_{\text{coef}} = 11$ $M = 10$, $N_{\text{coef}} = 21$ $M = 10$, $N_{\text{coef}} = 51$

Figure 2.9: FIR filter responses for a linear FM chirp for the number of subbands $M = 2$, 5, and 10, and the number of FIR coefficients $N_{\text{coef}} = 11$, 21, and 51 ($B =$ 100 MHz, $f_{\text{S}} = 200$ MHz, $\tau_p = 100$ μs).

It is observed that increasing the number of coefficients improves the filter characteristics and also the reconstructed pulse.

2.8 Noise

The sampled baseband noise is modeled using the random generator available in IDL. The amplitude is limited to the range between -1 and 1. Because the baseband signal is complex, both I-channel and Q-channel have independently sampled noise. To ensure that throughout all simulations the noise data remains the same, two datafiles are created with one datafile for the I-channel and one for the Q-channel.

Each datafile contains 10 million values, which is sufficient for 32 elevation channels with 312,500 time samples. In the baseline case, discussed in chapter 3, the number of time samples is 23,801. The variance of the noise for the two datafiles is shown in Fig. 2.10. In the figure, the noise variance is shown as function of the number of samples used in computing the noise variance. In both cases the variance becomes constant for a few hundred samples and more.

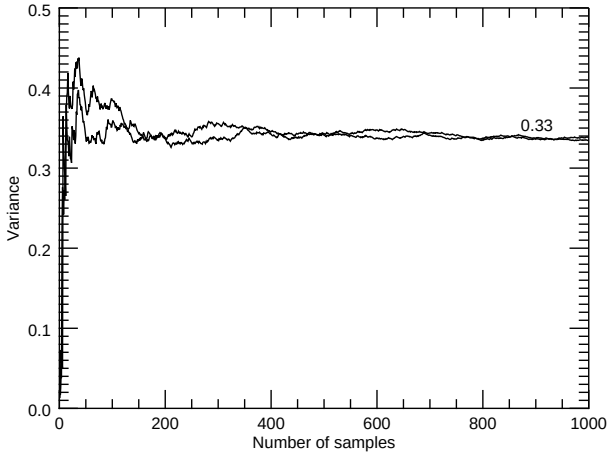

Figure 2.10: Noise variance versus number of samples used in the computation of the noise variance.

2.9 GRASP and antenna parameters

TICRA's GRASP [6] is used for simulation of the reflector antenna. GRASP uses the physical optics (PO) approximation to compute induced currents on scatterers. Using the computed currents, electromagnetic fields and antenna characteristics can be computed. In case of the reflector antenna considered in this thesis the feed illuminates a "scatterer". The scatterer considered here is the reflector, defined as a surface bounded by a rim. GRASP facilitates various surface definitions, such as predefined parabolic surfaces and surfaces with z-values tabulated on an xy grid. The rim defines the bounds of the surface and GRASP has several built-in rims and also allows for a rim defined in an xy plane. In Fig. 2.11 an example of a reflector antenna in GRASP is shown. In the top left corner the feed array and its local coordinate system are shown. The feed illuminates the reflector. The reflector is defined as a parabolic surface, bounded by a tabulated rim.

GRASP can output a variety of antenna parameters and electromagnetic results, such as currents. Here, the complex-valued antenna far field patterns belonging to each of the N_c elements is extracted. This can be further limited to only N_x elements when considering DBF in elevation only.

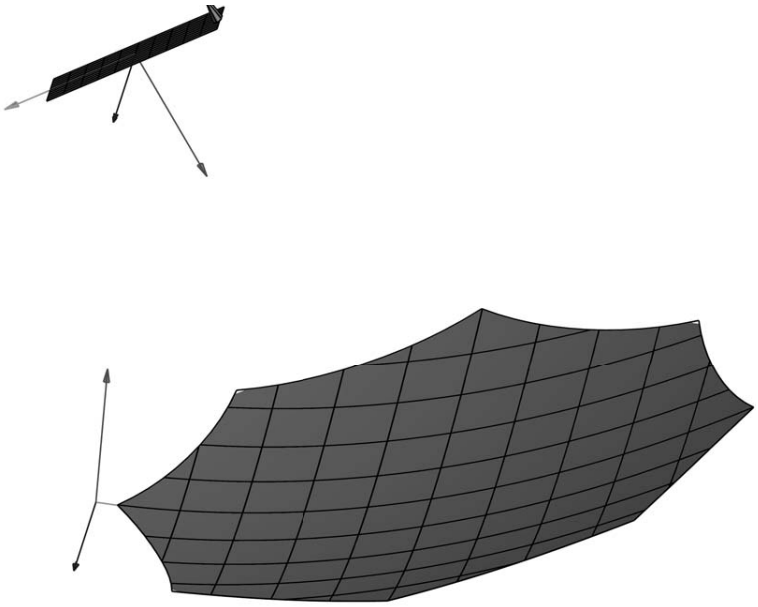

Figure 2.11: Example of a reflector antenna in GRASP. The surface of the reflector is parabolic, and bounded by the rim.

2.10 Conclusions and recommendations

This chapter introduces the computational model underlying the results for the subsequent chapters. The model applies SCORE DBF in elevation for a point target, using the MVDR technique to form the digital beams. The model also facilitates tracking of the pulse with M digital beams, in which each beam tracks a particular part of the pulse. To facilitate this operation, FIR filters are applied to the respective subbands. The number of FIR filter coefficients N_{coef} is an additional parameter in the computational model. In the following chapter, the case of a point scatterer at boresight is discussed with a reflector free from distortion. This case serves as a baseline for the chapter thereafter, as well as to investigate the impact of the number of beams and subbands M and the number of filter coefficients N_{coef} on DBF performance.

It is recommended that in a follow-up project, the model is expanded to include range ambiguities, beamforming in azimuth, as well as SAR imaging. Additionally, it would be useful if beamforming techniques other than MVDR are incorporated. These added features will facilitate further investigations and required trade-offs.

Chapter 3

Baseline case

In the previous chapter the computational model was described. In this chapter the model is applied to the specific case of a point scatterer at boresight and beamforming with a reflector antenna free of deformations. This specific case serves as the baseline case for the next chapter in which the impact of deformations in the reflector is investigated.

3.1 Parameters

The parameters used in the baseline are provided in Table 3.1. Most of the parameters are close to the currently assumed parameters of Tandem-L. However, the pulse duration τ_p of 100 μs is much larger than the pulse duration proposed for Tandem-L. This long pulse duration is used to investigate the impact of the use of subbands on the digital beamforming. When pulse durations become shorter, the effect is less distinguishable. The sample frequency f_s of 170 MHz is also higher than projected for Tandem-L.

Table 3.1: Parameters for the baseline case.

parameter	symbol	value
orbital height	h_s	740 km
boresight angle w.r.t. nadir	θ_bore	32.7°
focal length	F	13.5 m
number of elevation feed elements	N_x	32
center frequency	f_c	1.2575 GHz
chirp bandwidth	B	85 MHz
pulse duration	τ_p	100 μs
sample frequency	f_s	170 MHz

3.2 Reflector surface

The surface of the reflector is parabolic and defined by $z = (x^2 + y^2)/4F$, where F is the focal length. The GRASP surface file for the baseline case is defined with 200 points for $-10 \leq x \leq 10$ and with 200 points for $0 \leq y \leq 20$.

3.3 Reflector rim

Besides the definition of the surface, GRASP also requires the definition of the reflector rim. The definition of the reflector rim is first made in the $z = 0$ plane. Using this rim definition, GRASP determines the limits of the reflector surface by projecting the rim definition onto the parabolic surface. That is, the rim definition in the $z = 0$ plane determines the cut-out of the reflector through a projection of the rim on the reflector surface. Here, the definition of the reflector rim is provided by DLR and shown in Fig. 3.1.

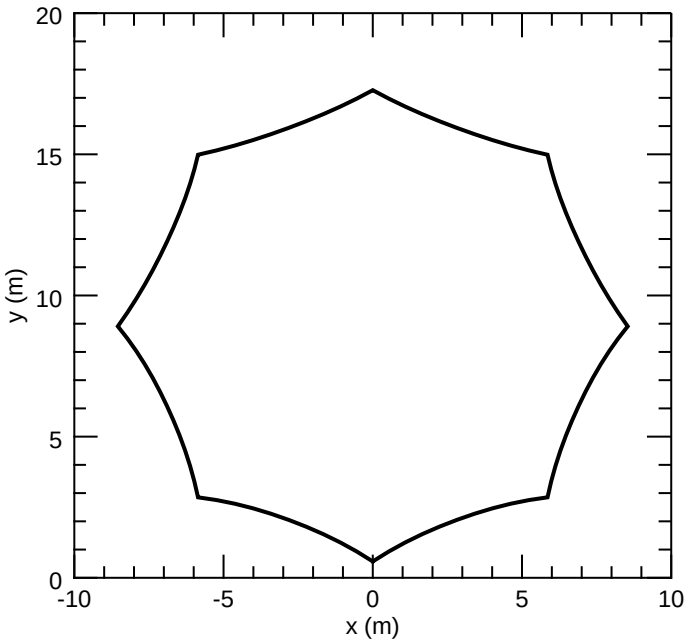

Figure 3.1: Definition of the rim.

3.4 Point scatterer

For the computation of the DBF parameters a point scatterer is assumed at boresight, i.e., at $\theta_{\text{bore}} = 32.7°$. The distance between the satellite and the point scatterer is 901.5 km and the roundtrip time is 6.014157 ms.

3.5 Antenna performance

In Fig. 3.2 the gain patterns for all 32 channels are shown. For the channels at boresight the maximum gain is around 43.2 dB. For channel 0 the maximum gain is 36.4 dB, and for channel 31 the maximum gain is 40.4 dB.

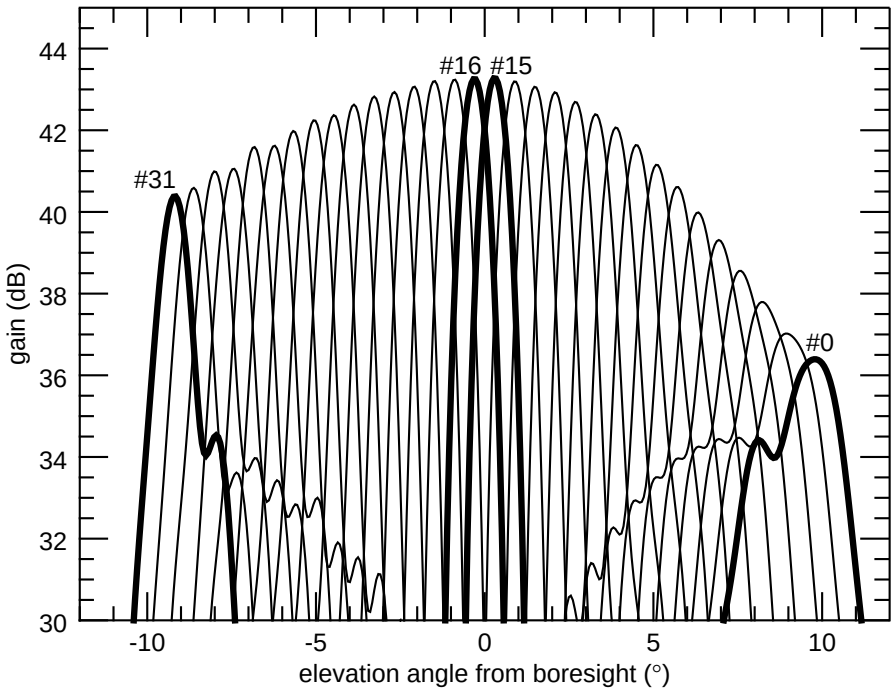

Figure 3.2: Antenna gain patterns of the 32 elevation channels in principal azimuth cut.

In Fig. 3.3 on the left the elevation is shown where the maximum gain occurs. Clearly, these elevations are neatly aligned between -10° and 10°. In the same figure on the right the beamwidth for all channels is shown. For most channels the beamwidth is 1.5° or less.

3.6 Sampling

In the computations, sampling starts 20 μs before the pulse and ends 20 μs after the pulse. Therefore, the total sampling time is 140 μs, and the number of samples is 23801 (140 μs $\times$ 170 MHz + 1).

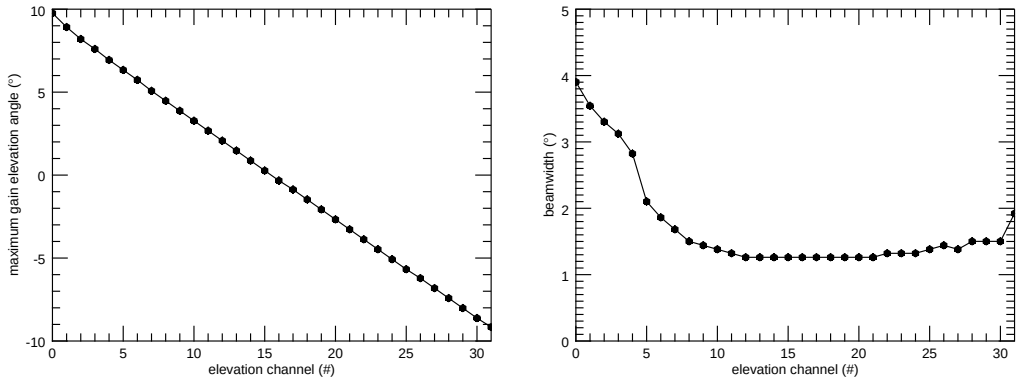

Figure 3.3: Left: elevation of maximum gain. Right: beamwidth.

3.7 DBF performance

3.7.1 Signal-to-noise ratio

The signal-to-noise ratio SNR at the output is provided in Table 3.2. The first observation is that the SNR for $N_{\text{coef}} = 1$ is substantially lower compared to larger values of N_{coef}. The second observation is that the SNR improves when the number of subbands M is increased and when the number of coefficients N_{coef} is increased. The best SNR is found in the lower right corner of the table for the combination $M = 20$ and $N_{\text{coef}} = 201$.

Table 3.2: Baseline case SNR (dB).

	M					
N_{coef}	1	2	5	10	15	20
1	44.339	41.198	41.613	41.626	41.628	41.628
5	47.632	47.766	47.848	47.837	47.835	47.833
11	47.438	48.237	48.614	48.635	48.636	48.636
21	47.416	48.327	48.677	48.699	48.700	48.700
51	47.398	48.363	48.690	48.725	48.734	48.735
101	47.395	48.368	48.699	48.731	48.737	48.740
151	47.390	48.375	48.702	48.736	48.741	48.744
201	47.389	48.376	48.702	48.702	48.742	48.746

3.7.2 Peak-sidelobe ratio

The peak-sidelobe ratio $PSLR$ is provided in Table 3.3. For each column the minimum $PSLR$ is underlined. For the case of one subband ($M = 1$) the $PSLR$ is large. In case of two subbands ($M = 2$) the $PSLR$ is very small. Increasing M further brings the $PSLR$ to around -13 dB. It is also observed that the largest number of

coefficients N_{coef} does not result in the largest *PSLR*. Instead, the largest *PSLR* is found for $N_{\text{coef}} \approx 2M$. For a pulse without any distortion due to DBF the computed *PSLR* is -13.300 dB.

Table 3.3: Baseline case *PSLR* (dB).

	M					
N_{coef}	1	2	5	10	15	20
1	-16.783	-8.900	-11.234	-11.432	-11.466	-11.478
5	-23.362	-2.648	-10.831	-11.268	-11.345	-11.371
11	-16.293	-2.020	-12.396	-12.922	-13.015	-13.047
21	-16.556	-2.063	-12.177	-13.051	-13.145	-13.178
51	-16.704	-2.060	-12.010	-12.975	-13.176	-13.208
101	-16.737	-2.062	-11.953	-12.956	-13.134	-13.187
151	-16.748	-2.062	-11.934	-12.947	-13.123	-13.188
201	-16.752	-2.062	-11.927	-12.941	-13.120	-13.182

3.7.3 Integrated sidelobe ratio

The *ISLR* is provided in Table 3.4. For each column the largest *ISLR* is underlined. For $M = 1$ the largest *ISLR* is found and for $M = 2$ the smallest *ISLR* is found. Increasing M further brings it to around -9 or -10 dB. The highest *ISLR* is found for $N_{\text{coef}} = 5$. For a pulse without any distortion due to DBF the computed *ISLR* is -9.679 dB.

Table 3.4: Baseline case *ISLR* (dB).

	M					
N_{coef}	1	2	5	10	15	20
1	-13.664	-6.980	-8.755	-8.895	-8.919	-8.928
5	-20.480	-2.834	-10.578	-10.942	-11.004	-11.025
11	-14.024	-2.145	-10.510	-10.911	-10.957	-10.972
21	-13.848	-1.495	-8.234	-10.135	-10.167	-10.175
51	-13.667	-1.243	-7.322	-9.216	-9.796	-9.814
101	-13.572	-1.148	-7.016	-8.961	-9.407	-9.525
151	-13.514	-1.114	-6.915	-8.853	-9.286	-9.459
201	-13.488	-1.099	-6.861	-8.785	-9.232	-9.396

3.7.4 Slant range resolution

The slant range resolution Δr is provided in Table 3.5. The slant range resolution is lowest for $M = 1$ and $M = 2$. For larger M and $N_{\text{coef}} = 1$ the resolution is around

1.54 m. For larger N_{coef} the slant range resolution is around 1.57 m. For a pulse without any distortion due to DBF the computed Δr is 1.558 m.

Table 3.5: Baseline case slant range resolution Δr (m).

	M					
N_{coef}	1	2	5	10	15	20
1	1.691	1.479	1.534	1.539	1.539	1.541
5	1.894	1.993	1.622	1.633	1.631	1.633
11	1.741	2.379	1.620	1.629	1.631	1.631
21	1.719	2.297	1.589	1.594	1.594	1.596
51	1.702	2.275	1.572	1.576	1.576	1.574
101	1.695	2.268	1.565	1.570	1.570	1.570
151	1.695	2.264	1.565	1.567	1.567	1.567
201	1.693	2.262	1.563	1.567	1.567	1.567

3.8 Conclusions and recommendations

In this chapter, SCORE DBF in elevation and the principal azimuth plane is applied to the baseline case of a point scatterer at boresight and a reflector free from deformations. First, the far field patterns of the 32 channels are computed in GRASP. The simulated boresight gain is around 43 dB, which is the maximum of all gains among the 32 channels. Then, the simultaneous influence of the number of subbands M and the number of FIR filter coefficients N_{coef} on four DBF parameters (*SNR*, *PSLR*, *ISLR*, and slant range resolution Δr) is investigated. From this investigation it is concluded that $M = 10$ subbands and $N_{\text{coef}} = 21$ will produce a good balance between computational effort required and the quality of the DBF parameters.

It is recommended that the analysis is repeated for point targets off boresight. It is anticipated that for point targets closer to nadir more subbands will be beneficial. And as the pulse propagates further, less subbands will be needed as the look angles of the respective digital beams get closer to each other. It is also recommended that the analysis is repeated for shorter pulse durations. Here a pulse duration of $\tau_p = 100$ μs is used to investigate the impact of M and N_{coef}. Tandem-L will use a pulse duration of $\tau_p = 10$ μs and it is anticipated that tracking this pulse requires less beams and less associated subbands.

Chapter 4

Impact of reflector deformation

4.1 Introduction

The impact of deformation of the reflector surface from the ideal parabolic surface is investigated in this chapter. More specifically, the impact on the following antenna parameters is investigated:

1. Maximum gain
2. Maximum gain elevation angle
3. Beamwidth

And the impact on the following DBF parameters for a point target at boresight is investigated:

1. *SNR*
2. *PSLR*
3. *ISLR*
4. Δr

The number of deformed reflector cases that can be reviewed is unlimited. Here, the discussion is restricted to two sets of cases, which are discussed in the following sections. The results of these cases are compared with the baseline case, established in chapter 3.

4.1.1 Definition of radius ρ and angle φ

The definition of radius ρ and angle φ is provided first. Both are used in the two sets of cases to define the deformation Δz. In Fig. 4.1 (left) the rim definition is shown again. In it, also a circle with radius $\rho_c = 8.5$ m is defined, centered at (0,8.9). This circle passes through the eight corner points of the rim. As shown in the figure, a point $P(x, y)$ lying within the circle can be defined in terms of the radius ρ and angle φ.

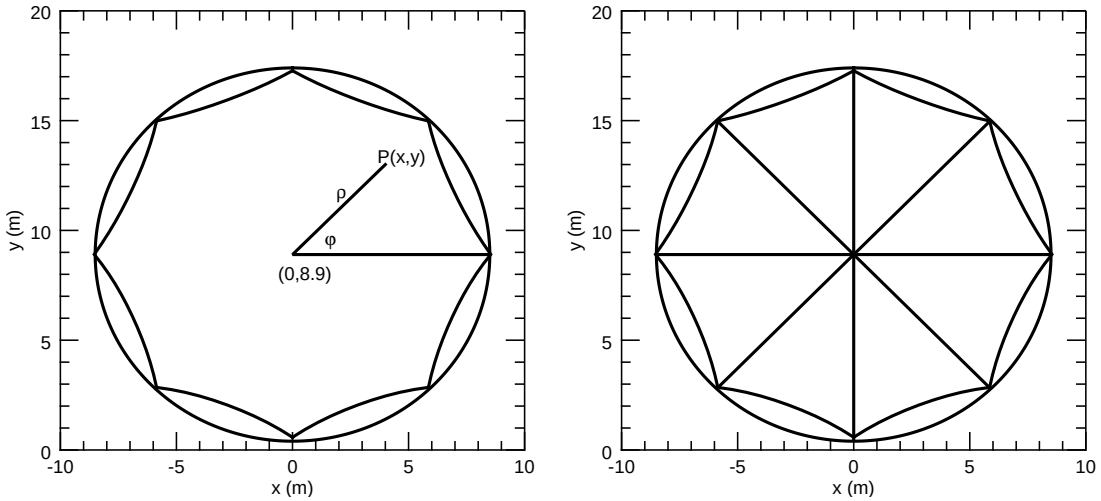

Figure 4.1: Definition of radius ρ and angle φ (left), and the eight ribs (right).

4.1.2 Deformations in radius and angle

The first set of cases uses the cylindrical coordinate system with radius ρ and angle φ to define the deformations. Sinusoidal deformations as a function of the radius ρ are first considered. Subsequently, a number of cases are considered with deformation in ρ and φ simultaneously.

4.1.3 Deformations unfurlable reflector

In the second set of cases an unfurlable type of reflector is considered. The center of the reflector is assumed at the center of the rim. Along the eight ribs of the antenna, shown in Fig. 4.1 on the right, zero deformation is assumed. Deformations of the reflector between the ribs are then considered.

4.1.4 Number of subbands and filter coefficients

In chapter 3 the impact of the number of subbands M and the number of filter coefficients N_{coef} on the digital beamforming performance is investigated. These two parameters should be sufficiently large to provide stable results, while keeping the computational burden reasonable. In the following, $M = 10$ and $N_{\text{coef}} = 21$ is used, unless otherwise noted. With these values, the MVDR weights are computed first for the baseline case. These weights are then applied to all cases of the deformed reflector. Through this approach the impact of the deformations on the beamforming is assessed.

4.2 Cosinusoidal in radius, invariant with angle

The deformation is modeled as cosinusoidal with radius ρ ($0 \leq \rho \leq \rho_c$) and invariant with angle φ:

$$\Delta z = A \cos\left(N_\rho \frac{\pi\rho}{2\rho_c}\right) \tag{4.1}$$

Two cases are considered:

1. $N_\rho = 1$
2. $N_\rho = 3$

4.2.1 $N_\rho = 1$

In case $N_\rho = 1$, a quarter-period cosinusoidal deformation between $\rho = 0$ and $\rho = \rho_c$ occurs, and there is no deformation with respect to the angle φ. Ten instances are simulated with A varying from -5 cm to 5 cm, in increments of 1 cm ($A = 0$ is the baseline case, which was simulated and discussed previously). In Fig. 4.2 the deformations of the two cases of A = -5 cm and A = 5 cm are shown. Note that the range in both x-direction and y-direction spans 20 m, while the maximum deformation in z is only 5 cm.

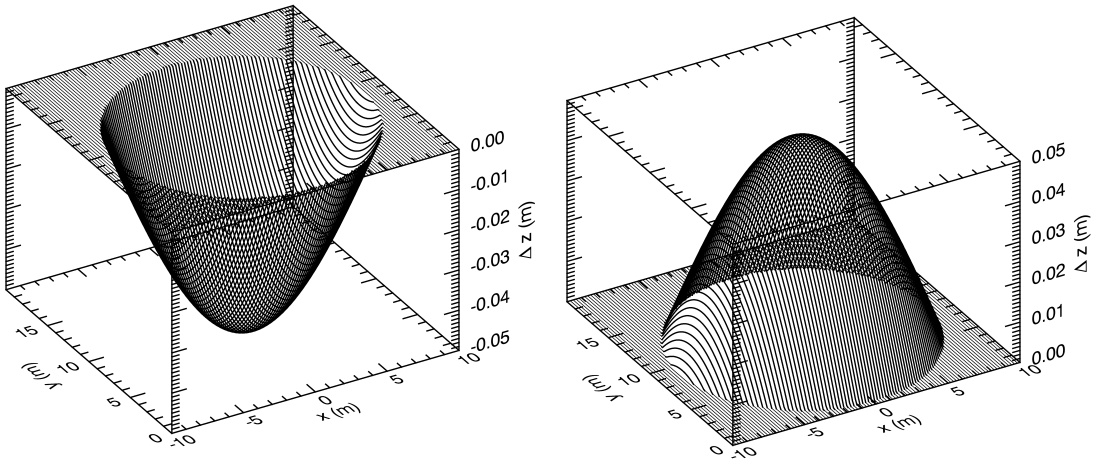

Figure 4.2: Deformations with amplitude A = -5 cm (left) and A = 5 cm (right).

Antenna parameters

In Fig. 4.3 the antenna gain patterns for the baseline case and the case of the deformed antenna with $A = 5$ cm are shown. The patterns for the deformed reflector are indicated by a thick line, and the baseline case by a normal line. In the top row the patterns for all 32 channels are shown, in the bottom row the gain patterns for channel 15 are shown. Reductions in maximum gain are clearly observed for almost

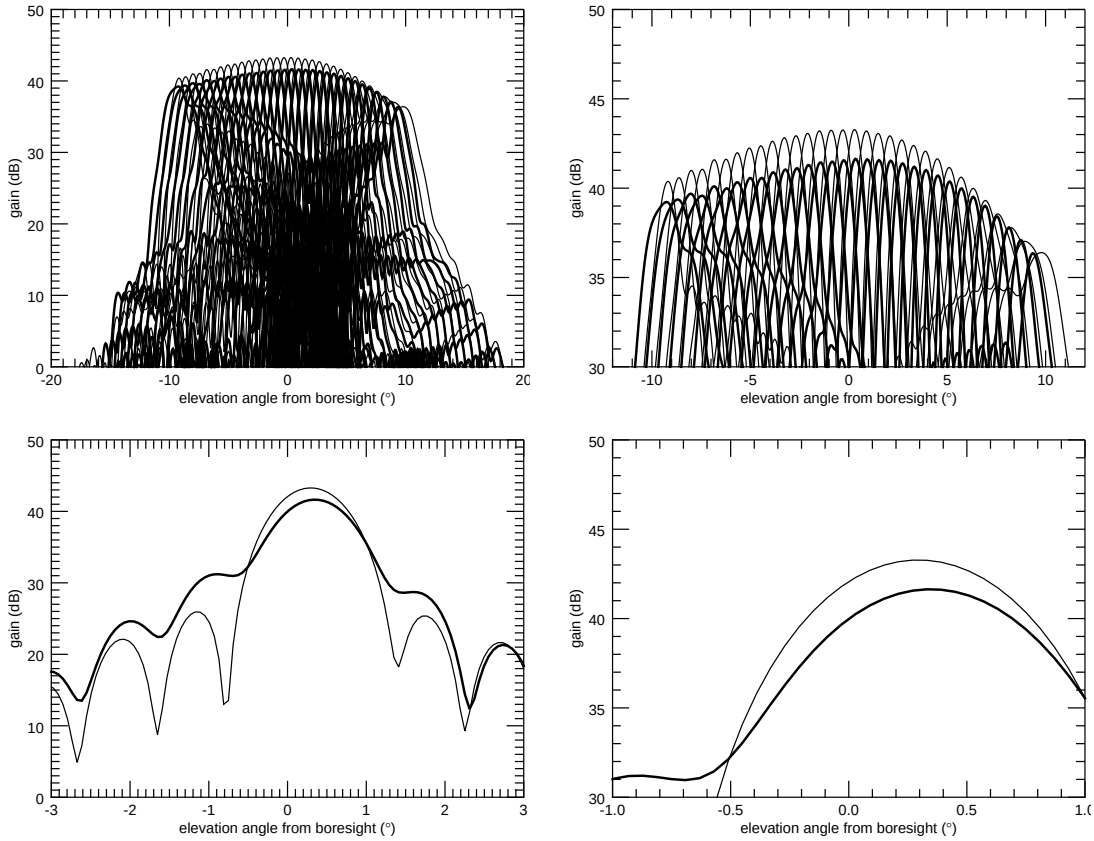

Figure 4.3: Gain patterns for deformed antenna (thick line) and baseline case. Top row: gain for all channels. Bottom row: gain for channel 15.

all channels. Elevations where the maximum gain occurs also change significantly for the lowest numbered channels. The beamwidth of the channels around boresight is hardly affected. However, beamwidth variations are found for the lower numbered channels and the higher numbered channels.

For channel 15 the gain drops 1.6 dB, and the elevation where the maximum gain occurs increases by less than 0.1°.
In Fig. 4.4 the difference with the antenna parameters of the baseline case are shown. The top row shows the changes in the maximum gain for each elevation channel. A positive change means that the gain has increased compared to the baseline case, and a negative change indicates a decrease compared to the baseline case. The middle row shows the change in the elevation angle where the maximum gain occurs. A positive value means that the elevation angle where the maximum gain occurs has increased and a negative value indicates that the elevation angle has decreased, i.e., the elevation angle has moved towards nadir. The bottom row shows the change in the beamwidth compared to the baseline case. A positive value indicates that the beamwidth has increased, a negative value indicates that the beamwidth has decreased. The three pictures in the left column are for the cases where the amplitude of the deformations at the center are from A = -1 ... -5 cm,

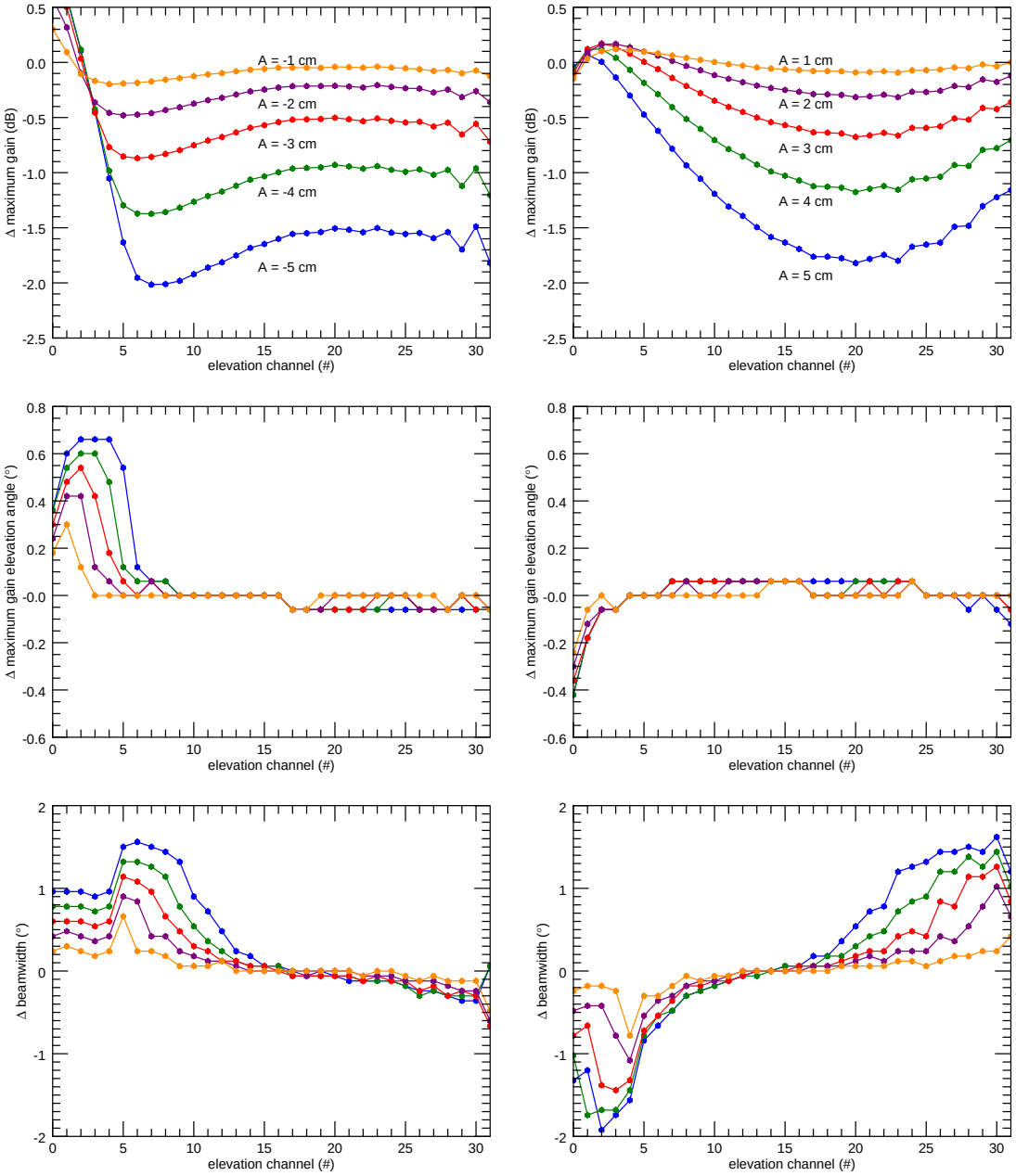

Figure 4.4: Deviation of antenna parameters. Top row: gain; middle row: maximum gain elevation; bottom row: beamwidth. Left column: A = -1 ... -5 cm. Right column: $A = 1 \ldots 5$ cm.

the three pictures in the right column are for $A = 1 \ldots 5$ cm.

The change in the maximum gain for cases where A is negative are different from the cases where A is positive. When A is negative the maximum change occurs in the lower numbered channels, whereas for positive A the maximum gain change occurs around channels 20-25. The elevations where the maximum gains occur are mostly unaffected, except for the lower numbered channels when A is negative.

The change in beamwidth is most pronounced for the first 12 channels when A is negative. When A is positive the changes occur at channels below 10 and above 20. Boresight channels are relatively unaffected.

DBF parameters

The DBF parameters are shown in Table 4.1. The *SNR* is clearly affected by the deformations. By comparing the *SNR* from the table with the antenna parameters for the elevation channels around boresight, shown in Fig. 4.4, a clear relationship is observed. A gain reduction of one dB in the channels around boresight results approximately in a one dB reduction in the *SNR*. It is important to keep in mind that the elevation angles where the maxima occur are mostly unaffected by the deformations. Later the impact of shifts in these angles are considered.

Interestingly, the *PSLR*, the *ISLR*, and the Δr are unaffected by the deformations. This is further discussed in section 4.7.

Table 4.1: DBF parameters for $N_\rho = 1$.

A (cm)	-5.0	-4.0	-3.0	-2.0	-1.0
Δ *SNR* (dB)	-1.65	-1.05	-0.59	-0.26	-0.07
Δ *PSLR* (dB)	0.00	0.00	0.00	0.00	0.00
Δ *ISLR* (dB)	0.00	0.00	0.00	0.00	0.00
Δ (Δ r) (m)	0.00	0.00	0.00	0.00	0.00

A (cm)	1.0	2.0	3.0	4.0	5.0
Δ *SNR* (dB)	-0.06	-0.24	-0.55	-1.00	-1.58
Δ *PSLR* (dB)	0.00	0.00	0.00	0.00	0.00
Δ *ISLR* (dB)	0.00	0.00	0.00	0.00	0.00
Δ (Δ r) (m)	0.00	0.00	0.00	0.00	0.00

4.2.2 $N_\rho = 3$

Secondly, the case of $N_\rho = 3$ is considered. In this case three quarter-periods cosinusoidal deformation between $\rho = 0$ and $\rho = \rho_c$ occur, and no deformation with respect to the angle. Ten instances are simulated with A varying from -5 cm to 5 cm, in increments of 1 cm ($A = 0$ is the baseline case, and not simulated here). In Fig. 4.5 the deformations of the two extreme cases of A = -5 cm and $A = 5$ cm are shown.

Antenna parameters

In Fig. 4.6 the changes in the antenna parameters are shown. The impact of the deformations on the gain of the antenna is very large. For deformations with $|A| =$ 5 cm, the gain is reduced by 5-6 dB for most channels. The impact on the elevations

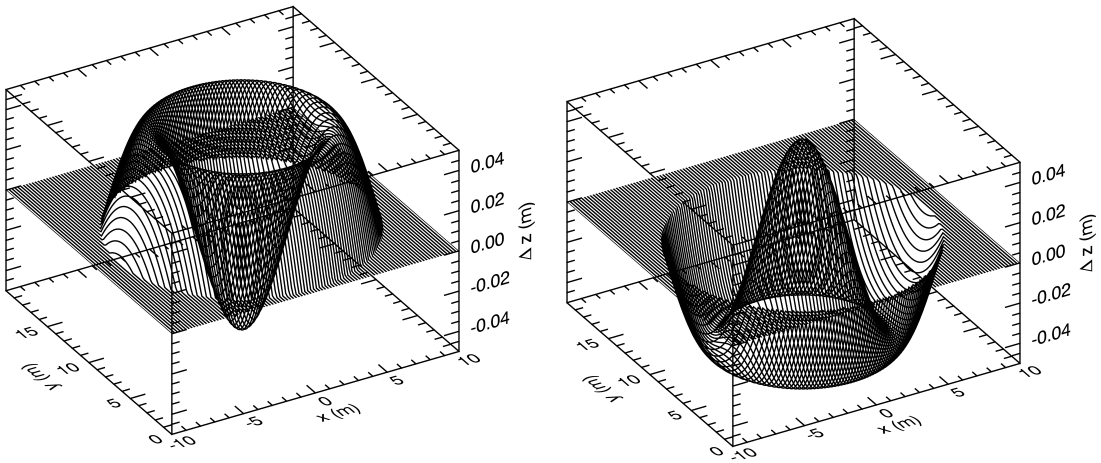

Figure 4.5: Deformations for $N_\rho = 3$ with amplitude A = -5 cm (left) and $A = 5$ cm (right).

where the maximum gains occur is not large. And impact on the beamwidth is clearly visible.

DBF parameters

In Table 4.2 the DBF parameters are shown. As in the previous case, the impact of the reflector deformation on the *PSLR*, *ISLR*, and the slant range resolution is very small. However, the impact on the *SNR* is again significant. Comparing the change in the maximum gain, shown in Fig. 4.6, with the change in the *SNR*, again a close relationship is observed. For example, for A = -5 cm the maximum gain for channels at boresight is reduced by 5 dB, and the *SNR* is reduced by 5.64 dB.

Table 4.2: DBF parameters for $N_\rho = 3$.

A (cm)	-5.0	-4.0	-3.0	-2.0	-1.0
Δ *SNR* (dB)	-5.64	-4.13	-2.47	-1.12	-0.28
Δ *PSLR* (dB)	-0.01	0.00	0.00	0.00	0.00
Δ *ISLR* (dB)	0.00	0.00	0.00	0.00	0.00
Δ (Δr) (m)	0.00	0.00	0.00	0.00	0.00

A (cm)	1.0	2.0	3.0	4.0	5.0
Δ *SNR* (dB)	-0.28	-1.10	-2.43	-4.08	-5.58
Δ *PSLR* (dB)	0.00	0.00	0.00	-0.01	-0.01
Δ *ISLR* (dB)	0.00	0.00	0.00	0.00	0.00
Δ (Δr) (m)	0.00	0.00	0.00	0.00	0.00

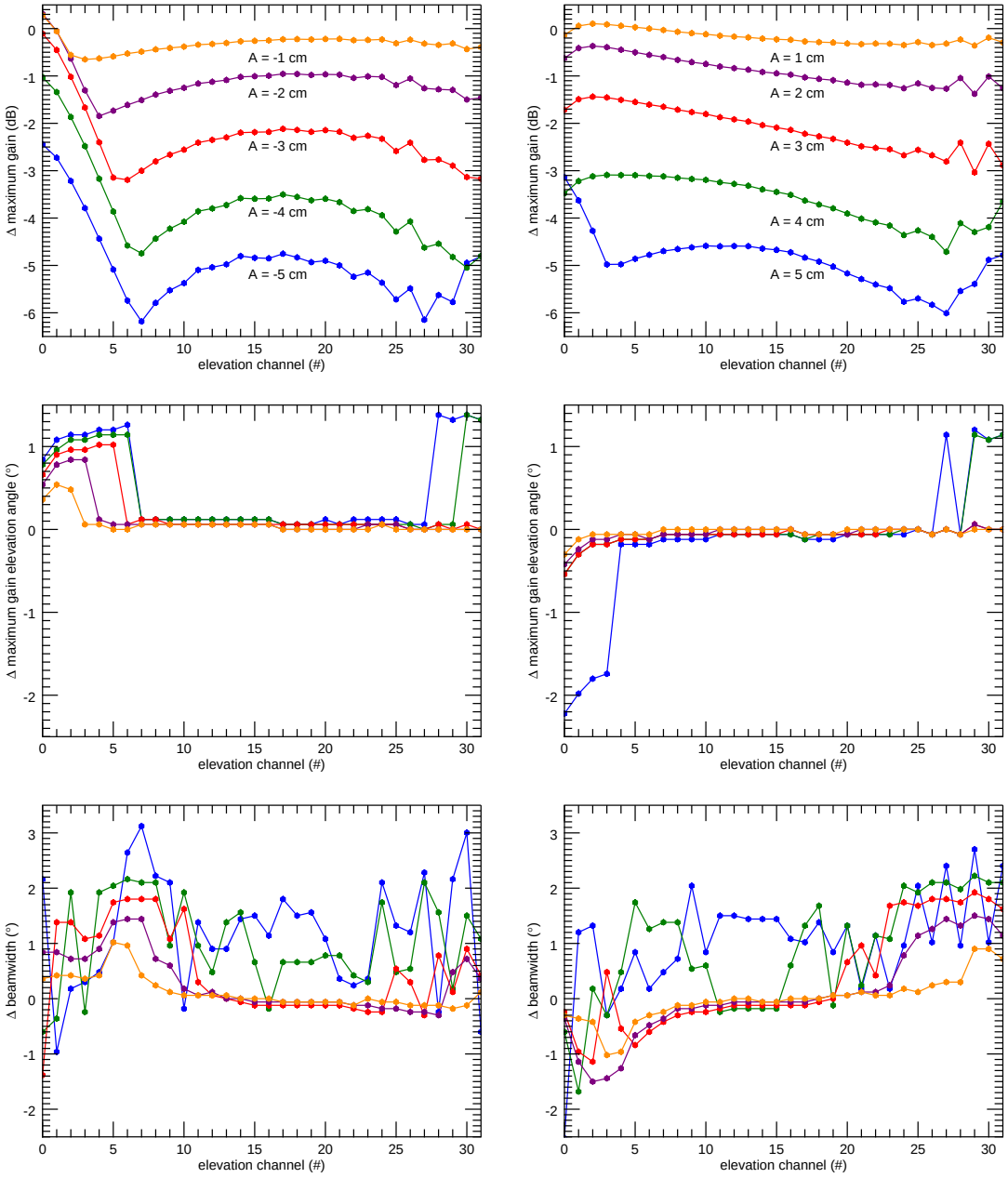

Figure 4.6: Change of antenna parameters for $N_\rho = 3$.. Top row: gain; middle row: maximum gain elevation; bottom row: beamwidth. Left column: A = -1 ... -5 cm. Right column: $A = 1 \ldots 5$ cm.

4.3 Sinusoidal in radius, cosinusoidal in angle

The deformation is modeled as sinusoidal with radius ρ and cosinusoidal with angle φ:

$$\Delta z = A \sin\left(N_\rho \frac{\pi\rho}{2\rho_c}\right) \cos\left(N_\varphi \frac{\varphi}{2}\right) \tag{4.2}$$

In this case, the deformation at the center of the circle is always zero. This could represent the case where the center of the reflector is fixated. The following four cases are considered:

1. $N_\rho = 2$ and $N_\varphi = 0$
2. $N_\rho = 2$ and $N_\varphi = 2$
3. $N_\rho = 4$ and $N_\varphi = 0$
4. $N_\rho = 4$ and $N_\varphi = 2$

4.3.1 $N_\rho = 2$ and $N_\varphi = 0$

In case $N_\rho = 2$ and $N_\varphi = 0$, a half-period sinusoidal deformation between $\rho = 0$ and $\rho = \rho_c$ occurs, and there is no deformation with respect to the angle φ. Ten instances are simulated in GRASP with A varying from -5 cm to 5 cm, in increments of 1 cm (as before, $A = 0$ is the baseline case). In Fig. 4.7 the deformations for the two extreme cases of A = -5 cm and $A = 5$ cm are shown. As noted at the start of this section, there is no deformation at the center of the circle. This could represent the case where this particular point is fixated in the reflector.

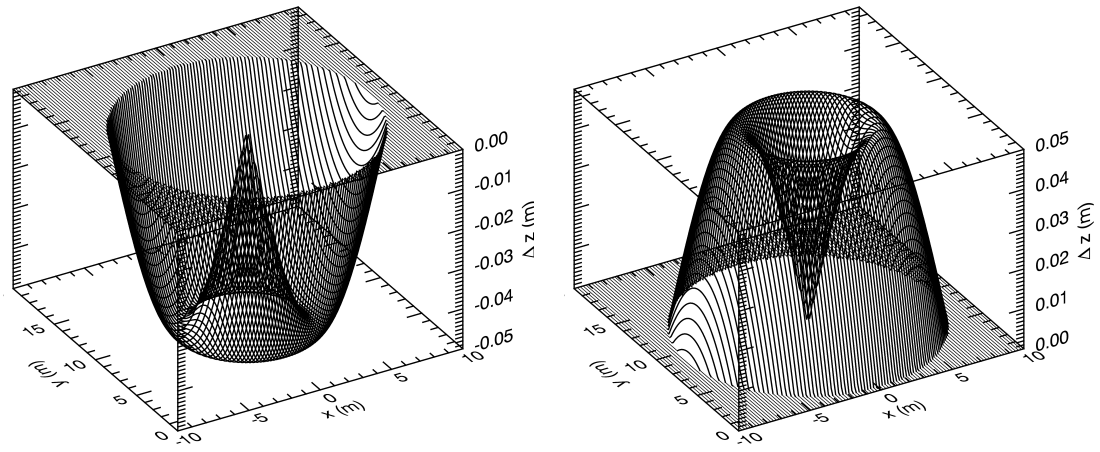

Figure 4.7: Deformations for $N_\rho = 2$, $N_\varphi = 0$, with amplitude A= -5 cm (left) and $A = 5$ cm (right).

Antenna parameters

In Fig. 4.8 the impact of the deformations on the antenna parameters is shown. A deterioration in the maximum gains of around 1.3 dB is observed for the channels at boresight for $|A| = 5$ cm. Changes in the elevation angles where the maximum gains occur of 0.06°-0.12° are found for most channels. The beamwidth also changes, but is fairly unaffected for the channels at boresight.

DBF parameters

The impact on the DBF parameters is shown in Table 4.3. As in the previous case, the *SNR* is impacted by the deformation. For deformations with $|A| = 5$ cm, the gain is reduced by 1.3 dB. And, as before, there is a relationship between the reduction in *SNR*, and the reduction in maximum gain. The other DBF parameters are hardly affected by the deformations.

Table 4.3: DBF parameters for $N_\rho = 2$, $N_\varphi = 0$.

A (cm)	-5.0	-4.0	-3.0	-2.0	-1.0
Δ *SNR*(dB)	-1.35	-0.87	-0.49	-0.22	-0.06
Δ *PSLR*(dB)	0.00	0.00	0.00	0.00	0.00
Δ *ISLR*(dB)	0.00	0.00	0.00	0.00	0.00
Δ (Δ r) (m)	0.00	0.00	0.00	0.00	0.00

A (cm)	1.0	2.0	3.0	4.0	5.0
Δ *SNR*(dB)	-0.05	-0.20	-0.47	-0.84	-1.32
Δ *PSLR*(dB)	0.00	0.00	0.00	0.00	0.00
Δ *ISLR*(dB)	0.00	0.00	0.00	0.00	0.00
Δ (Δ r) (m)	0.00	0.00	0.00	0.00	0.00

4.3.2 $N_\rho = 2$ and $N_\varphi = 2$

Second, the case of $N_\rho = 2$ and $N_\varphi = 2$ is considered. In this case a half-period sinusoidal deformation between $\rho = 0$ and $\rho = \rho_c$ occurs, and there is one period of sinusoidal deformation with respect to the angle φ. Ten instances are simulated with A varying from -5 cm to 5 cm, in increments of 1 cm ($A = 0$ is the baseline case). In Fig. 4.9 the deformations of the two extreme cases of A = -5 cm and A = 5 cm are shown.

Antenna parameters

In Fig. 4.10 the changes in the antenna parameters are shown.

The first, important, observation is that the results for the cases A = -1 ... -5 cm are the same as for the cases A = 1 ... 5 cm.

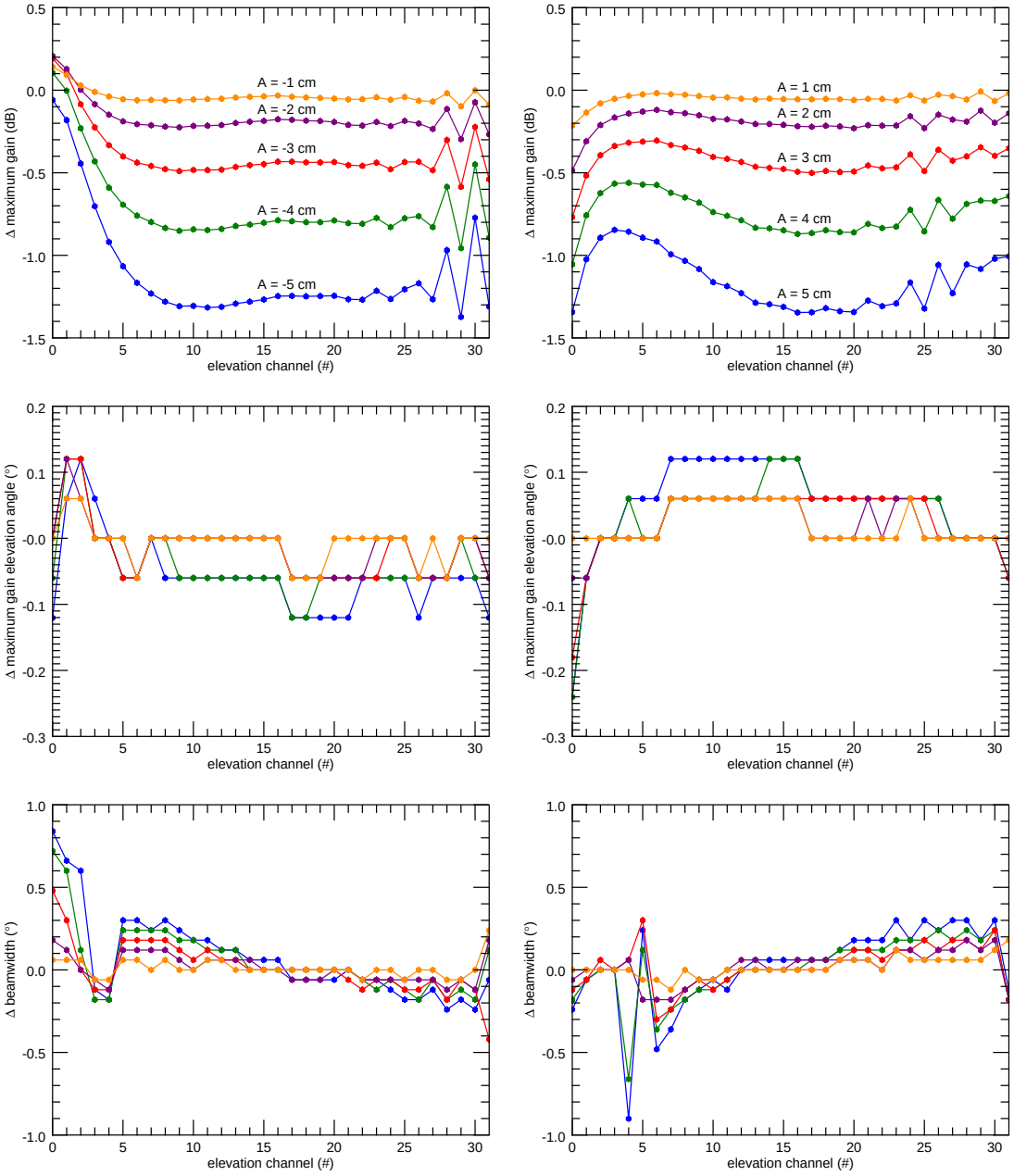

Figure 4.8: Deviation of antenna parameters for $N_\rho = 2$, $N_\varphi = 0$. Top row: gain; middle row: maximum gain elevation; bottom row: beamwidth. Left column: A = -1 ... -5 cm. Right column: $A = 1 \ldots 5$ cm.

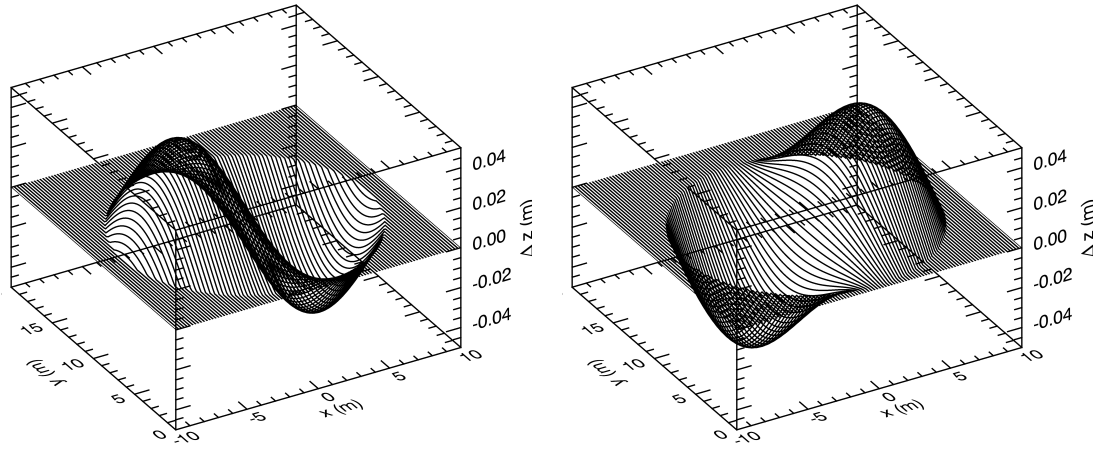

Figure 4.9: Deformations for $N_\rho = 2$, $N_\varphi = 2$ with amplitude A= -5 cm (left) and $A = 5$ cm (right).

The impact on the antenna parameters for deformations of 1 cm is low. However, the impact on the maximum gain is very large, especially for deformations of 4 cm and 5 cm. The impact on the elevation where the maximum gain occurs is small for most channels. The change in the beamwidth is in the order of a few tenth of a degree for most elevation channels. However, for $|A| = 5$ cm large fluctuations are observed.

DBF parameters

The DBF parameters are shown in Table 4.4. A very large impact on the *SNR* is observed for the larger deformations. The other DBF parameters are hardly affected.

Table 4.4: DBF parameters for $N_\rho = 2$, $N_\varphi = 2$.

A (cm)	-5.0	-4.0	-3.0	-2.0	-1.0
Δ *SNR*(dB)	-9.56	-5.51	-2.91	-1.24	-0.30
Δ *PSLR*(dB)	-0.02	-0.01	0.00	0.00	0.00
Δ *ISLR*(dB)	0.00	0.00	0.00	0.00	0.00
Δ (Δ r) (m)	0.00	0.00	0.00	0.00	0.00

A (cm)	1.0	2.0	3.0	4.0	5.0
Δ *SNR*(dB)	-0.30	-1.24	-2.91	-5.51	-9.56
Δ *PSLR*(dB)	0.00	0.00	0.00	-0.01	-0.02
Δ *ISLR*(dB)	0.00	0.00	0.00	0.00	0.00
Δ (Δ r) (m)	0.00	0.00	0.00	0.00	0.00

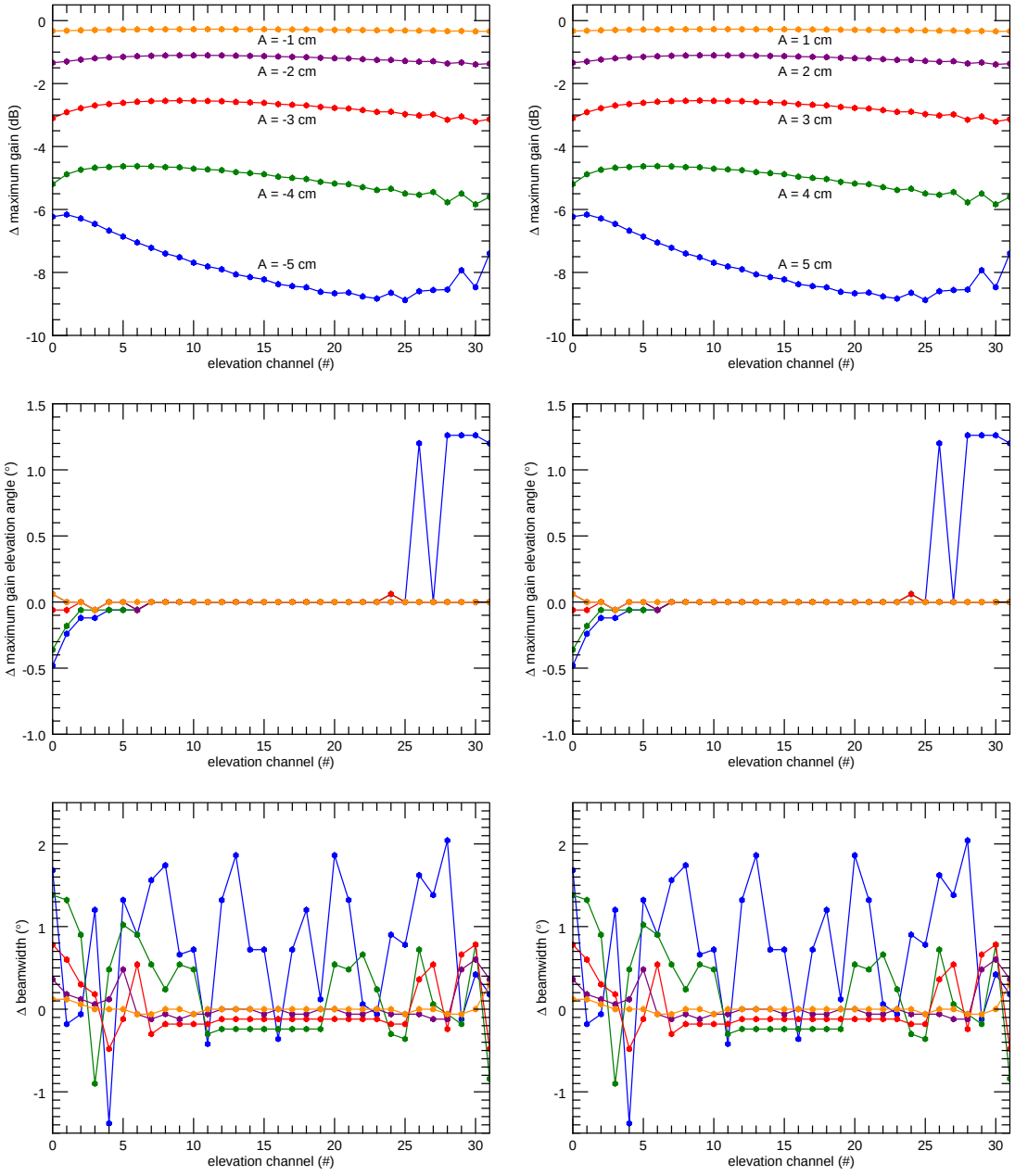

Figure 4.10: Deviation of antenna parameters for $N_\rho = 2$, $N_\varphi = 2$. Top row: gain; middle row: maximum gain elevation; bottom row: beamwidth. Left column: A = -1 ... -5 cm. Right column: $A = 1 \ldots 5$ cm.

4.3.3 $N_\rho = 4$ and $N_\varphi = 0$

In case $N_\rho = 4$ and $N_\varphi = 0$ a complete period sinusoidal deformation between $\rho = 0$ and $\rho = \rho_c$ occurs, and there is no deformation with respect to the angle φ. Ten instances are simulated with A varying from -5 cm to 5 cm, in increments of 1 cm ($A = 0$ is the baseline case). In Fig. 4.11 the deformations of the two extreme cases of A = -5 cm and $A = 5$ cm are shown.

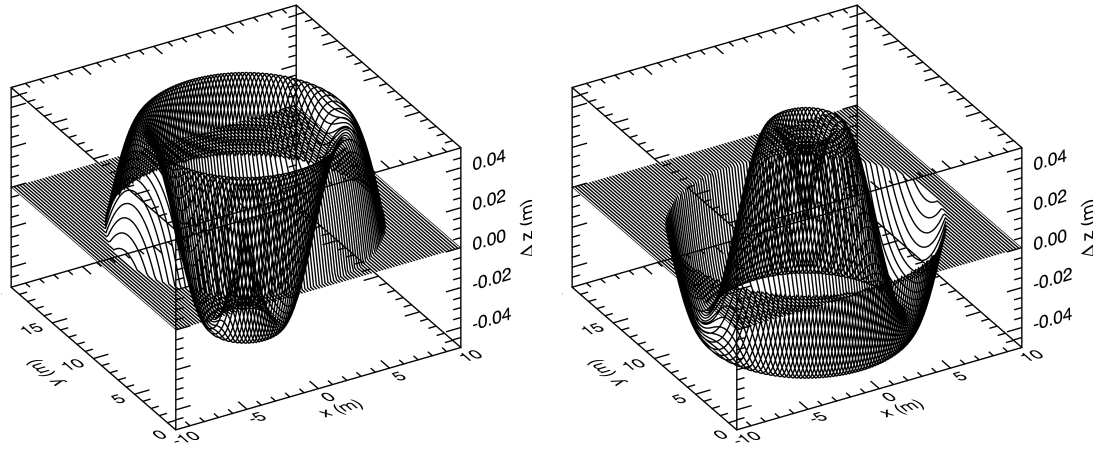

Figure 4.11: Deformations for $N_\rho = 4$, $N_\varphi = 0$, with amplitude A = -5 cm (left) and $A = 5$ cm (right).

Antenna parameters

In Fig. 4.12 the changes in the antenna parameters are shown.
The impact of the deformations on the maximum gains are again very significant. Gain deteriorations of more than 9 dB are observed for some channels for the larger deformations. The impact on the elevations where the maximum gains occur is also large for many channels for the larger deformations. Finally, relatively large changes in the beamwidth are also found for most channels and most deformations.

DBF parameters

The DBF parameters are provided in Table 4.5. Large changes in the *SNR* are observed, especially for the larger deformations. The impact on the other DBF parameters is again very small.

4.3.4 $N_\rho = 4$ and $N_\varphi = 2$

Finally, the case of $N_\rho = 4$ and $N_\varphi = 2$ is considered. In this case a complete period sinusoidal deformation between $\rho = 0$ and $\rho = \rho_c$ occurs, and there is one period of cosinusoidal deformation with respect to the angle φ. Ten instances are simulated

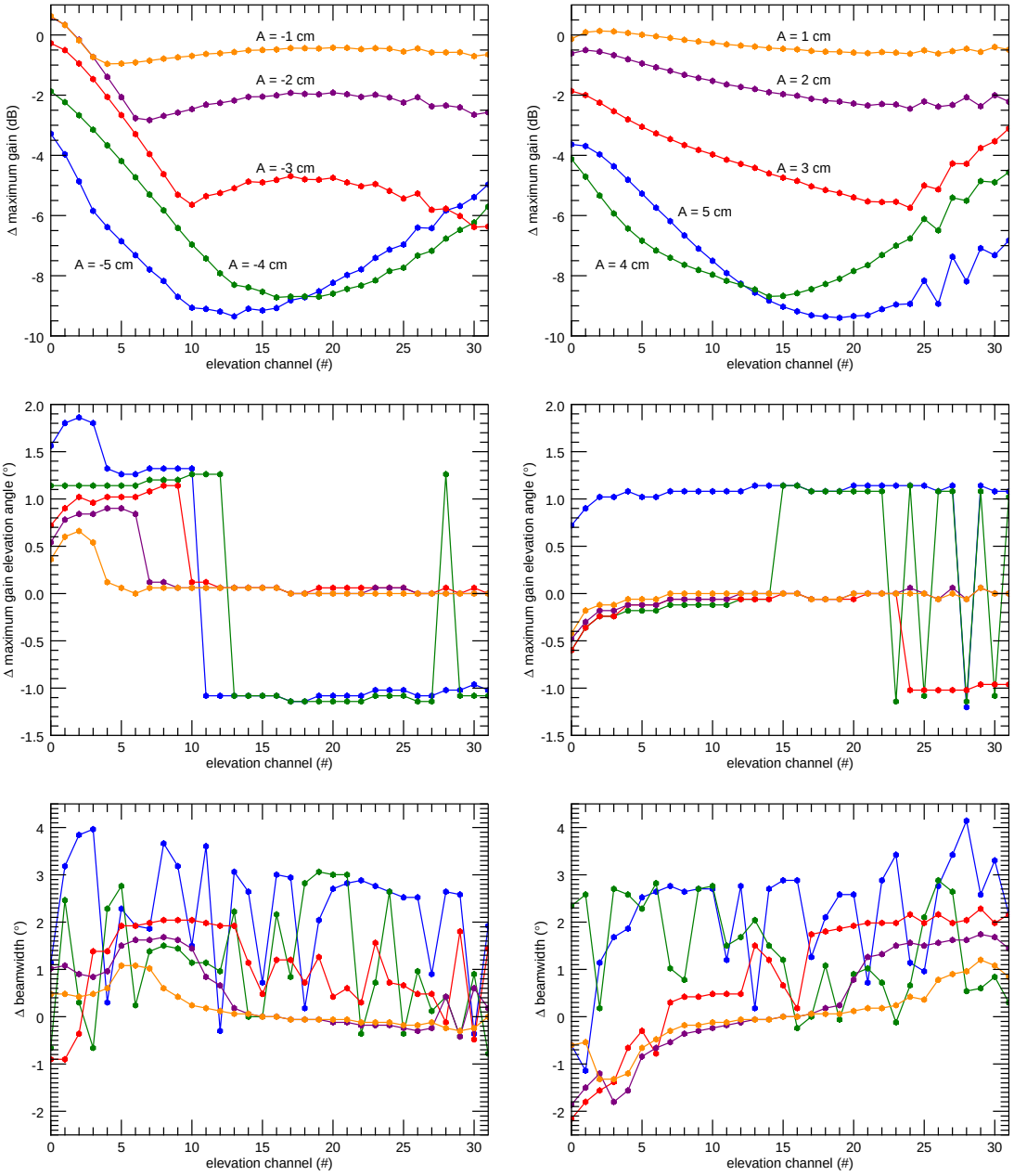

Figure 4.12: Deviation of antenna parameters for $N_\rho = 4$, $N_\varphi = 0$. Top row: gain; middle row: maximum gain elevation; bottom row: beamwidth. Left column: A = -1 ... -5 cm. Right column: $A = 1 \ldots 5$ cm.

Table 4.5: DBF parameters for $N_\rho = 4$, $N_\varphi = 0$.

A (cm)	-5.0	-4.0	-3.0	-2.0	-1.0
Δ SNR(dB)	-14.34	-10.48	-5.24	-2.16	-0.52
Δ $PSLR$(dB)	-0.05	0.00	0.00	0.00	0.00
Δ $ISLR$(dB)	0.00	0.00	0.00	0.00	0.00
Δ (Δr) (m)	0.00	0.00	0.00	0.00	0.00

A (cm)	1.0	2.0	3.0	4.0	5.0
Δ SNR(dB)	-0.50	-2.10	-5.14	-10.29	-14.32
Δ $PSLR$(dB)	0.00	0.00	0.00	-0.01	-0.04
Δ $ISLR$(dB)	0.00	0.00	0.00	0.00	0.00
Δ (Δr) (m)	0.00	0.00	0.00	0.00	0.00

with A varying from -5 cm to 5 cm, in increments of 1 cm ($A = 0$ is the baseline case). In Fig. 4.13 the deformations of the two extreme cases of A = -5 cm and A = 5 cm are shown.

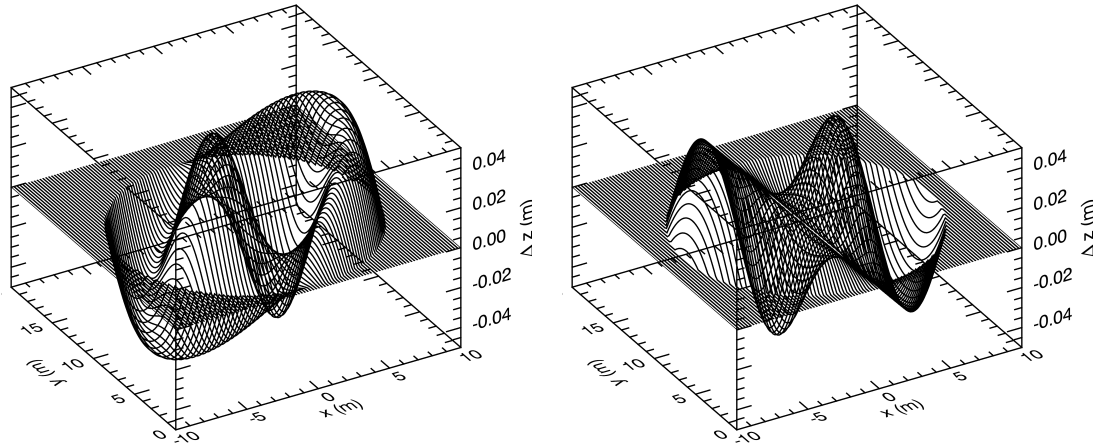

Figure 4.13: Deformations for $N_\rho = 4$, $N_\varphi = 2$ with amplitude A= -5 cm (left) and A = 5 cm (right)

Antenna parameters

In Fig. 4.14 the changes in the antenna parameters are shown.
The first observation is that the results for A = -1 ... -5 cm are the same as for A = 1 ... 5 cm. The impact on the maximum gain is again large, especially for the larger deformations. The changes in the elevations where the maximum gains occur are very small. Finally, moderate changes in the beamwidth are found for most of the deformations.

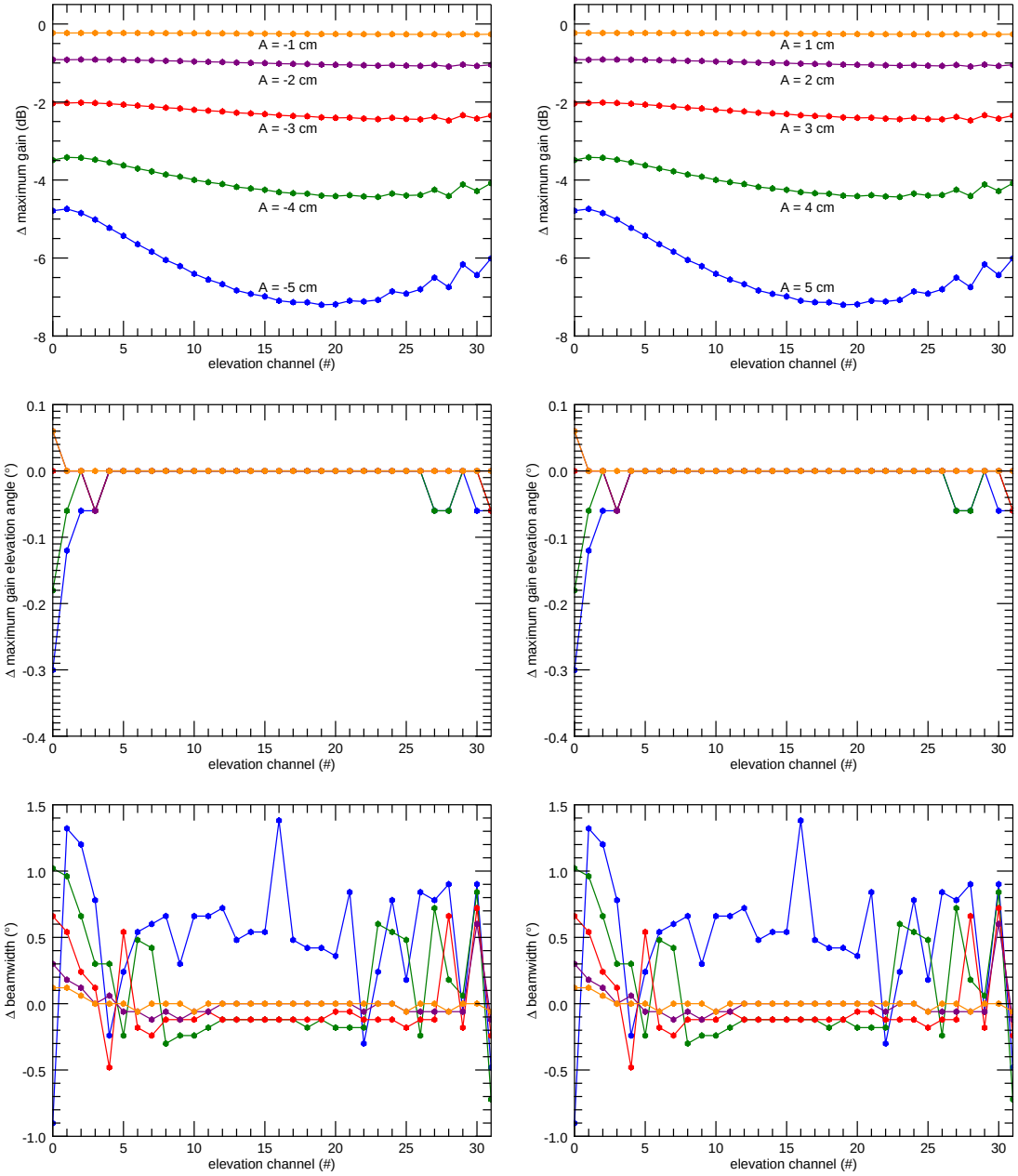

Figure 4.14: Deviation of antenna parameters for $N_\rho = 4$, $N_\varphi = 2$. Top row: gain; middle row: maximum gain elevation; bottom row: beamwidth. Left column: A = -1 ... -5 cm. Right column: $A = 1 \ldots 5$ cm.

DBF parameters

In Table 4.6 the DBF parameters are shown. The impact of the deformations on the *SNR* is large. Also, the relation between the deterioration of the maximum gain and the deterioration of the *SNR* is found again. The other DBF parameters are mostly unaffected.

Table 4.6: DBF parameters for for $N_\rho = 4$, $N_\varphi = 2$.

A (cm)	-5.0	-4.0	-3.0	-2.0	-1.0
Δ *SNR*(dB)	-7.86	-4.70	-2.53	-1.09	-0.27
Δ *PSLR*(dB)	-0.01	0.00	0.00	0.00	0.00
Δ *ISLR*(dB)	0.00	0.00	0.00	0.00	0.00
Δ (Δ r) (m)	0.00	0.00	0.00	0.00	0.00

A (cm)	1.0	2.0	3.0	4.0	5.0
Δ *SNR*(dB)	-0.27	-1.09	-2.53	-4.70	-7.86
Δ *PSLR*(dB)	0.00	0.00	0.00	0.01	-0.01
Δ *ISLR*(dB)	0.00	0.00	0.00	0.00	0.00
Δ (Δ r) (m)	0.00	0.00	0.00	0.00	0.00

4.4 Sinusoidal in radius and angle

The deformation is modeled as sinusoidal with radius ρ and sinusoidal with angle φ:

$$\Delta z = A \sin\left(N_\rho \frac{\pi\rho}{2\rho_c}\right) \sin\left(N_\varphi \frac{\varphi}{2}\right) \tag{4.3}$$

Two cases are considered:

1. $N_\rho = 2$ and $N_\varphi = 2$
2. $N_\rho = 4$ and $N_\varphi = 2$

4.4.1 $N_\rho = 2$ and $N_\varphi = 2$

In case $N_\rho = 2$ and $N_\varphi = 2$, a half-period sinusoidal deformation between $\rho = 0$ and $\rho = \rho_c$ occurs, and there is a full period sinusoidal deformation with respect to the angle φ. Ten instances are simulated with A varying from -5 cm to 5 cm, in increments of 1 cm ($A = 0$ is the baseline case). In Fig. 4.15 the deformations of the two extreme cases of A = -5 cm and $A = 5$ cm are shown.

Antenna parameters

In Fig. 4.16 the changes in the antenna parameters are shown.
The impact on the antenna gain is not as large as some of the other cases. Nevertheless, the impact is still significant. The impact on the elevation where the maximum gain occurs is clearly visible. An increase in the deformations results in an increase of the elevation of maximum gain for all channels. It is also noted that these changes in elevation are large. Impact on the beamwidth is also clearly visible, especially for the larger deformations.

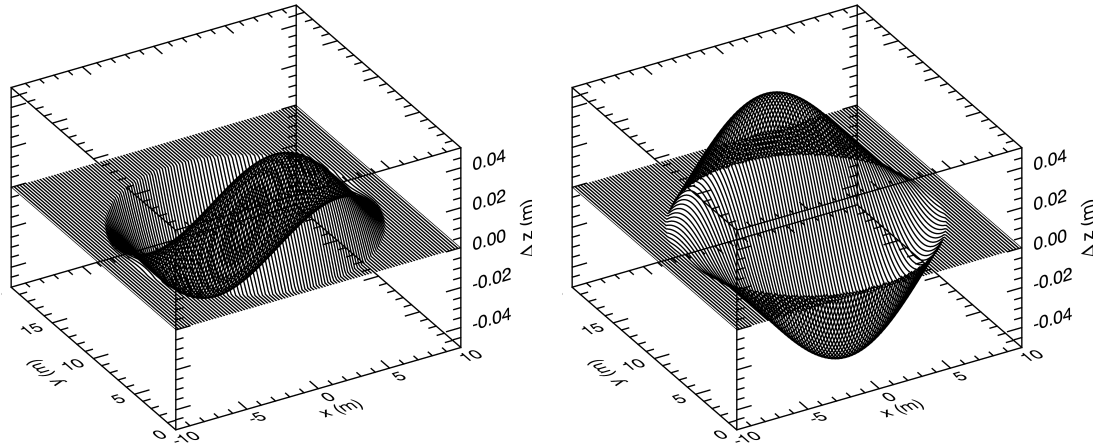

Figure 4.15: Deformations for $N_\rho = 2$ and $N_\varphi = 2$ with amplitude A= -5 cm (left) and $A = 5$ cm (right).

DBF parameters

The DBF parameters are shown in Table 4.7. Very large changes in the *SNR* are observed. For example, a change of more than 9 dB is found for deformations with $|A| = 5$ cm, whereas the gain drop is les than 3 dB. In section 4.7.1 it is shown that this large drop in *SNR* is due to the offset in elevation. Changes less than 0.1 dB in *PSLR* and *ISLR* are found, and no impact on Δr.

Table 4.7: DBF parameters for for $N_\rho = 2$ and $N_\varphi = 2$.

A (cm)	-5.0	-4.0	-3.0	-2.0	-1.0
Δ *SNR*(dB)	-9.20	-5.38	-2.85	-1.22	-0.30
Δ *PSLR*(dB)	0.03	0.01	0.00	0.00	0.00
Δ *ISLR*(dB)	0.06	0.02	0.01	0.00	0.00
Δ (Δ r) (m)	0.00	0.00	0.00	0.00	0.00

A (cm)	1.0	2.0	3.0	4.0	5.0
Δ *SNR*(dB)	-0.30	-1.23	-2.87	-5.39	-9.22
Δ *PSLR*(dB)	0.00	0.01	0.01	0.03	0.06
Δ *ISLR*(dB)	0.00	0.01	0.02	0.04	0.08
Δ (Δ r) (m)	0.00	0.00	0.00	0.00	0.00

4.4.2 $N_\rho = 4$ and $N_\varphi = 2$

Lastly, the case of $N_\rho = 4$ and $N_\varphi = 2$ is considered. In this case a full period of sinusoidal deformation between $\rho = 0$ and $\rho = \rho_c$ occurs, and there is a full period

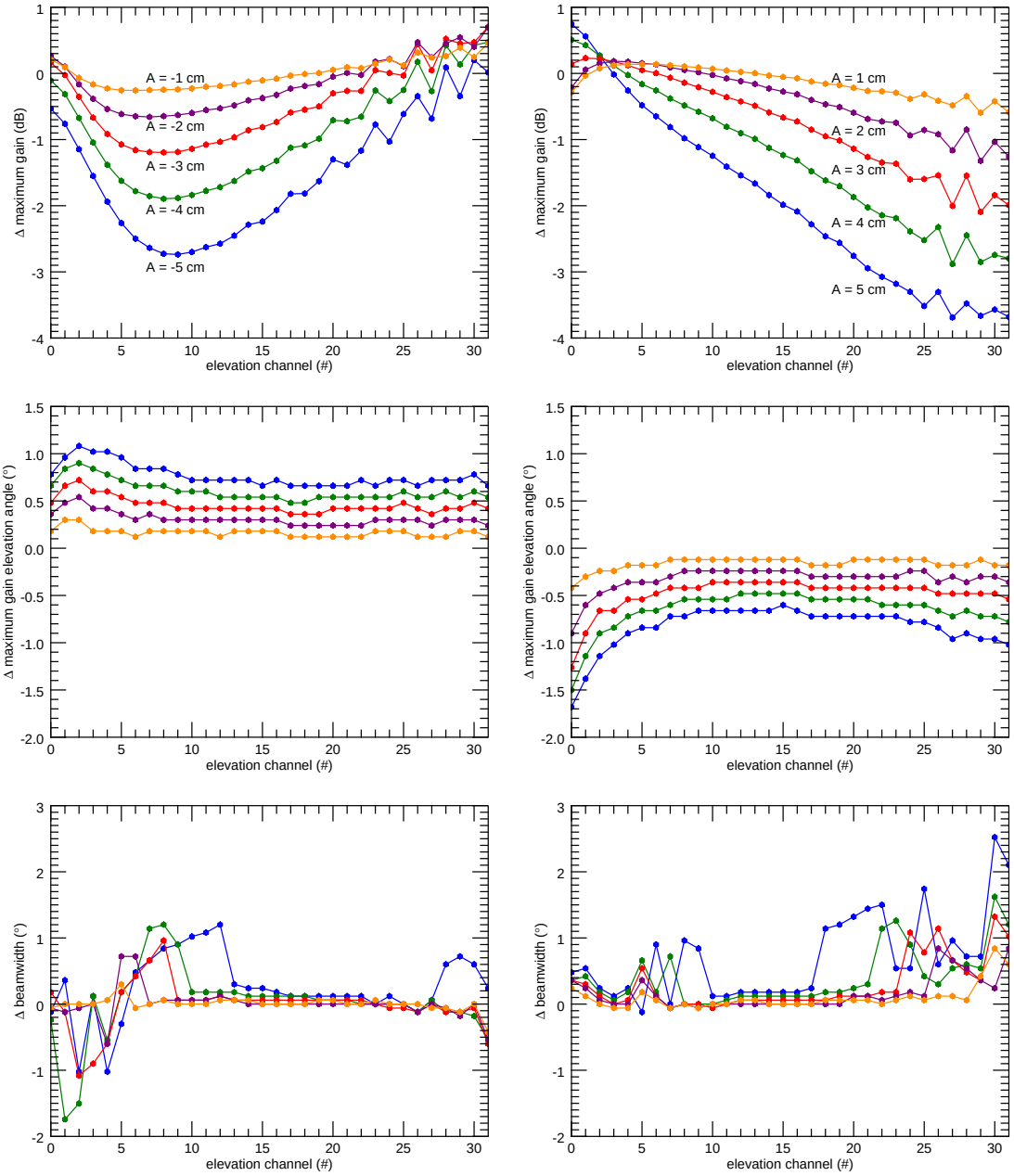

Figure 4.16: Change in antenna parameters for $N_\rho = 2$ and $N_\varphi = 2$. Top row: gain; middle row: maximum gain elevation; bottom row: beamwidth. Left column: A = -1 ... -5 cm. Right column: $A = 1 \ldots 5$ cm.

of sinusoidal deformation with respect to the angle φ. Ten instances are simulated with A varying from -5 cm to 5 cm, in increments of 1 cm ($A = 0$ is the baseline case). In Fig. 4.17 the deformations of the two extreme cases of A = -5 cm and A = 5 cm are shown.

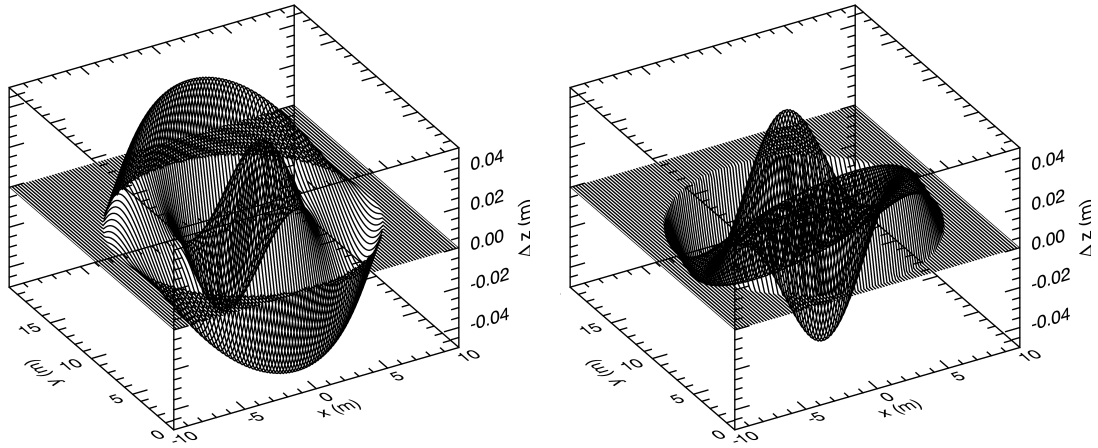

Figure 4.17: Deformations for $N_\rho = 4$, $N_\varphi = 2$ with amplitude A = -5 cm (left) and $A = 5$ cm (right)

Antenna parameters

In Fig. 4.18 the changes in the antenna parameters are shown.
The impact of the deformations on the maximum gain is relatively large; for $|A| =$ 5 cm the drop in the gain is 4-5 dB for most channels. Relatively large changes in the elevations where the maximum gain occurs are also found. The impact on the beamwidth is moderate for the smaller deformations. However, large changes are found for the larger deformations.

DBF parameters

The DBF parameters are shown in Table 4.8. As in the previous case, very large decreases in the *SNR* are found. For $|A| = 5$ cm the *SNR* deteriorates more than 7 dB, which is much larger than the drop in maximum gain of 4-5 dB. In section 4.7.1 it is shown that this large drop in *SNR* is due to the offset in elevation.

4.5 Cosinusoidal in radius, constant arc length

Previously, deformations cosinusoidal with radius ρ and invariant with angle φ ($N_\varphi = 0$) were considered for the cases of $N_\rho = 1$ and $N_\rho = 3$. Here, that exploration is extended by increasing N_ρ further, i.e., $N_\rho = 1$, 3, 5, 7, 9, ... The amplitude of the deformation is adjusted for each case such that the arc length along the deformation for ρ from 0 to ρ_c remains constant. To achieve that, for the case of $N_\rho = 1$ a maximum deformation of 5 cm is considered. The maximum deformation of all other cases then becomes 5 cm/N_ρ. In Fig. 4.19 the deformations are shown for $N_\rho = 5$, with an amplitude of 1 cm, and for $N_\rho = 9$, with an amplitude of 5.5 mm.

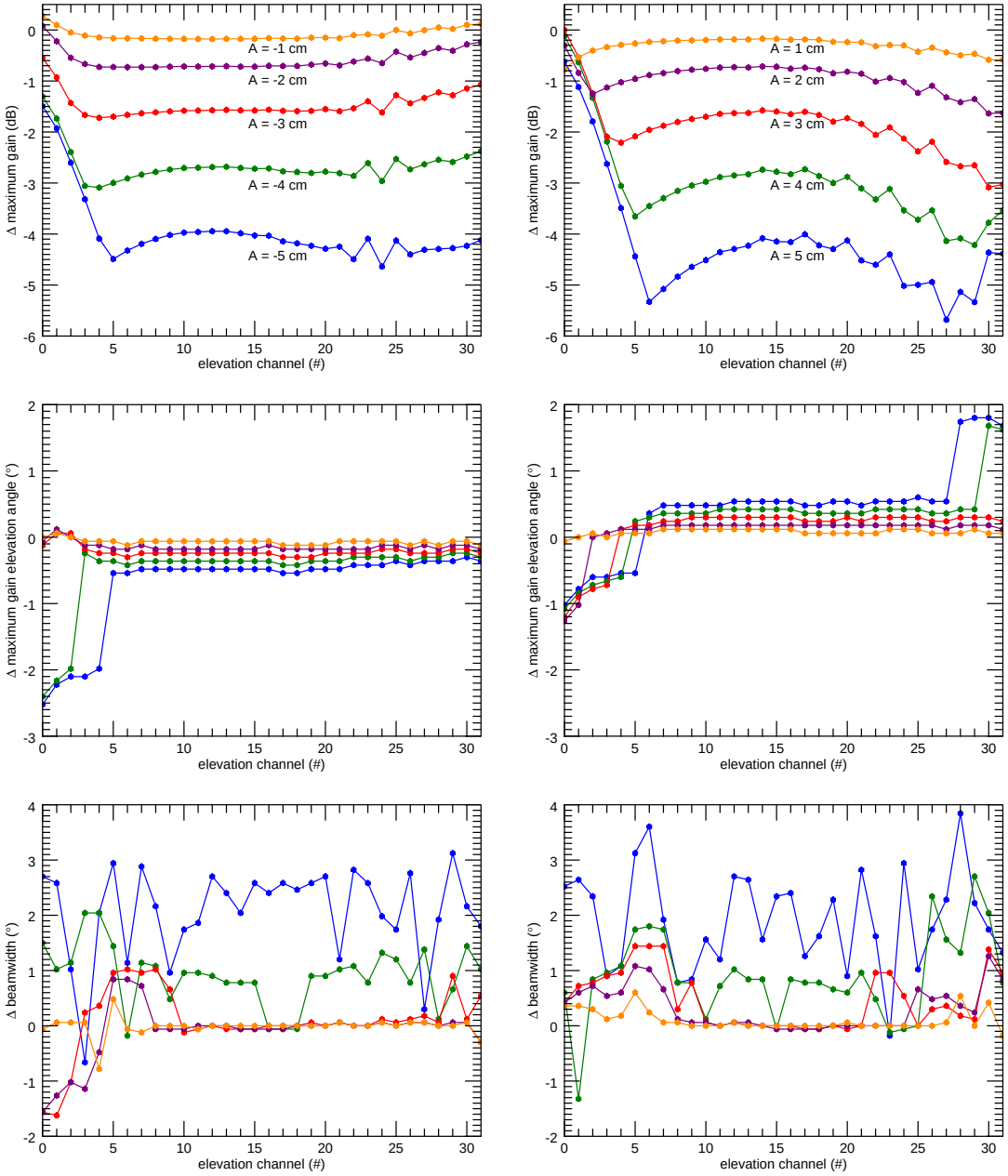

Figure 4.18: Deviation of antenna parameters for $N_\rho = 4$, $N_\varphi = 2$. Top row: gain; middle row: maximum gain elevation; bottom row: beamwidth. Left column: A = -1 ... -5 cm. Right column: $A = 1 \ldots 5$ cm.

Antenna parameters

In Fig. 4.20 the changes in the maximum gain are shown for $N_\rho = 1$, 3, 5, 7, 9, and 25. The first observation is that the change in maximum gain is largest for the case $N_\rho = 1$. The drop in gain is 1.5 dB or more for elevation channels 13 to 27. The second observation is that the reduction in maximum gain diminishes as N_ρ

Table 4.8: DBF parameters for $N_\rho = 4$, $N_\varphi = 2$.

A (cm)	-5.0	-4.0	-3.0	-2.0	-1.0
Δ *SNR*(dB)	-7.18	-4.38	-2.38	-1.03	-0.25
Δ *PSLR*(dB)	0.03	0.02	0.01	0.00	0.00
Δ *ISLR*(dB)	0.02	0.01	0.00	0.00	0.00
Δ (Δ r) (m)	0.00	0.00	0.00	0.00	0.00

A (cm)	1.0	2.0	3.0	4.0	5.0
Δ *SNR*(dB)	-0.26	-1.04	-2.39	-4.39	-7.19
Δ *PSLR*(dB)	0.00	0.00	0.01	0.01	0.03
Δ *ISLR*(dB)	0.00	0.00	0.00	0.01	0.02
Δ (Δ r) (m)	0.00	0.00	0.00	0.00	0.00

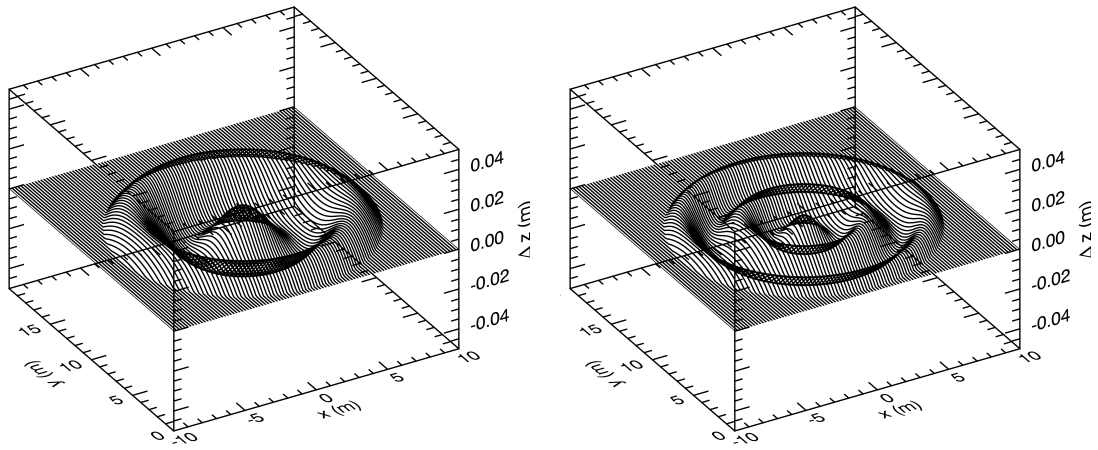

Figure 4.19: Deformations for $N_\rho = 5$ ($A = 1$ cm) and $N_\rho = 9$ ($A = 5.5$ mm).

increases. For $N_\rho = 9$ the drop in gain is not more than 0.2 dB for all channels. The last observation is that the drop in maximum gain becomes negligible for much larger N_ρ. The figure shows that for $N_\rho = 25$ the reflector almost behaves like a perfect parabolic reflector. Although not shown here, simulations for N_ρ up to 49 were performed and the results confirm the observation. The results for the elevation where the maximum gain occurs and the beamwidth are not shown here. But similar observations are made as for the maximum gain. For larger N_ρ the results converge to the reflector without deformation.

4.6 Unfurlable reflector

In the second set of deformations, the impact of deformations of an unfurlable reflector is considered. The setup uses the rim definition discussed previously. Also,

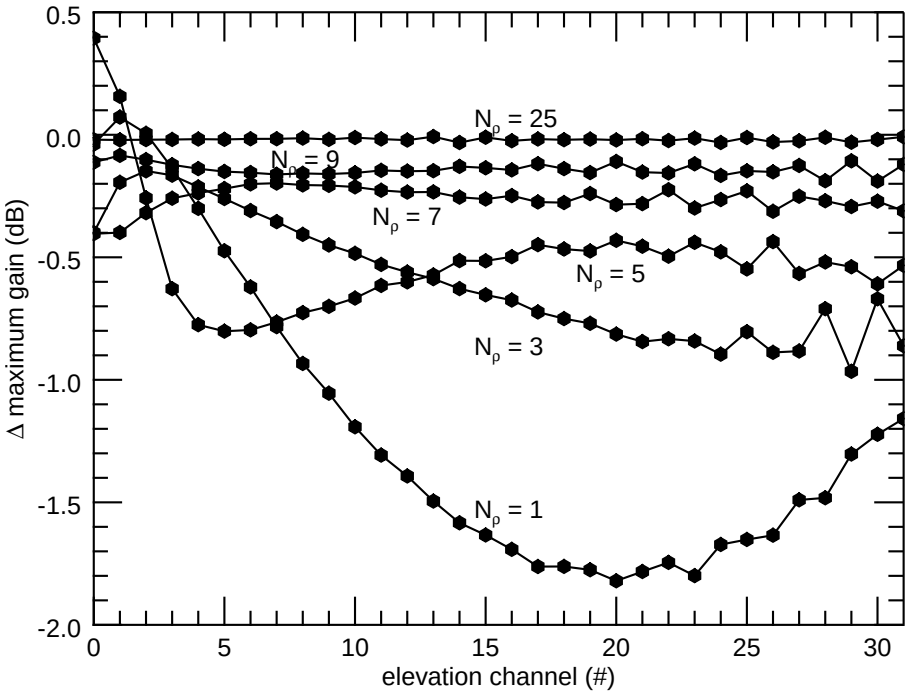

Figure 4.20: Maximum gain for cosinusoidal deformations and for N_ρ 1, 3, 5, 7, 9, and 25.

the radius ρ and angle φ, defined previously, are used again. Eight ribs are defined that support the unfurlable reflector, as shown in Fig. 4.21. The length of each of the eight ribs is ρ_c. It is assumed that no deformation occurs along these ribs, and that deformations do occur between the ribs.

The angle of each rib i w.r.t. the x-axis is denoted by φ_i, and the eight ribs are approximately 45° apart. The deformation considered here between rib i and rib $i+1$ is given by:

$$\Delta z = A \sin\left(\frac{\pi\rho}{2\rho_c}\right) \sin\left(\pi \frac{\varphi - \varphi_i}{\varphi_{i+1} - \varphi_i}\right) \tag{4.4}$$

Going from $\rho = 0$ to $\rho = \rho_c$ the deformation is sinusoidal, and between the ribs the deformation is also sinusoidal with angle φ. The maximum deformation occurs between two ribs when $\rho = \rho_c$. Ten instances are simulated with A varying from -5 cm to 5 cm, in increments of 1 cm ($A = 0$ is the baseline case, discussed previously). In Fig. 4.22 the deformed unfurlable reflector surfaces of two cases are shown. On the left a case is shown where the surface bulges outward between the ribs, and on the right the surface bulges inward. Note that in both cases, for illustration purposes, $|A| = 50$ cm. This is ten times larger than the largest case actually considered here.

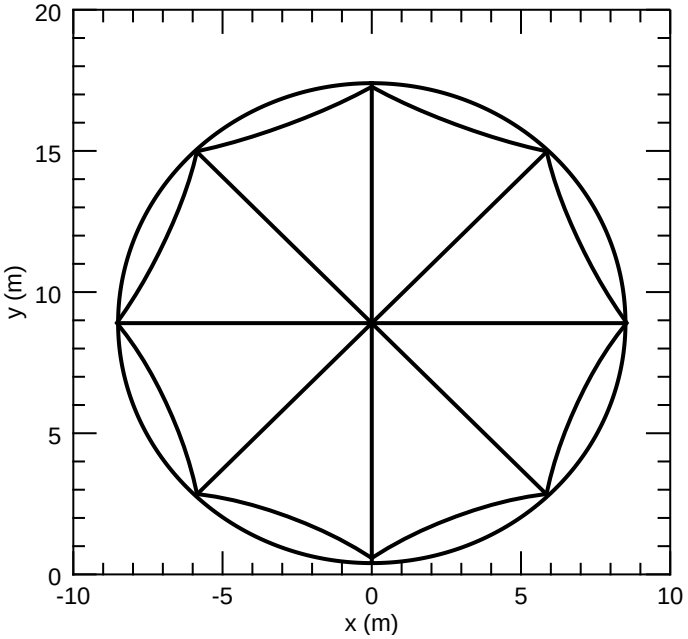

Figure 4.21: Definition of the rim and eight ribs.

Antenna parameters

The impact of the deformations on the antenna parameters is shown in Fig. 4.23. Impact on the maximum antenna gain is clearly visible, with a reduction in gain of 2 dB for some of the elevation channels when $|A| = 5$ cm. The impact on the elevations where the maximum gain occurs is not very large. The impact on the beamwidth varies from being small for the channels around boresight, and increasing for the channels away from boresight.

DBF parameters

In Table 4.9 the DBF parameters for the deformed unfurlable reflector are shown. As in most previous cases, the *SNR* is affected by the deformation, and the other DBF parameters are not affected.

4.7 Discussion

4.7.1 Impact of elevation offset

In several cases, shifts in elevation where the maximum gain occurs due to deformations are observed. The impact of such shifts can be significant, as illustrated in the following. Consider the case of three elevation channels with gain patterns versus elevation as shown in Fig. 4.24 on the left.

Suppose that for MVDR beamforing a set of weights is computed based on the gain at the elevation shown with the round dot. Because only the middle channel

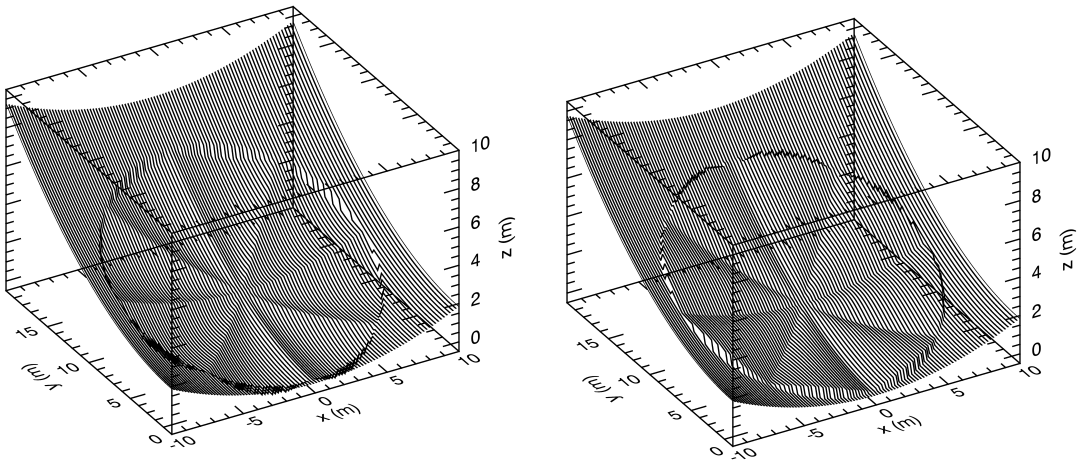

Figure 4.22: Deformed unfurlable reflector surface with amplitude A = -50 cm (left) and A = 50 cm (right).

Table 4.9: DBF parameters for the unfurlable reflector.

A (cm)	-5.0	-4.0	-3.0	-2.0	-1.0
Δ *SNR* (dB)	-1.78	-1.13	-0.63	-0.28	-0.07
Δ *PSLR* (dB)	0.00	0.00	0.00	0.00	0.00
Δ *ISLR* (dB)	0.00	0.00	0.00	0.00	0.00
Δ (Δ r) (m)	0.00	0.00	0.00	0.00	0.00

A (cm)	1.0	2.0	3.0	4.0	5.0
Δ *SNR* (dB)	-0.07	-0.27	-0.62	-1.12	-1.77
Δ *PSLR* (dB)	0.00	0.00	0.00	0.00	0.00
Δ *ISLR* (dB)	0.00	0.00	0.00	0.00	0.00
Δ (Δ r) (m)	0.00	0.00	0.00	0.00	0.00

has gain at that elevation, the computed weights will be 100% at that channel and 0% at the other two channels.

Suppose that the only impact of the reflector deformation is a shift in elevation of the gain patterns, as shown in Fig. 4.24 on the right. Because the same weights as previously computed are used, the beamforming uses 100% of the middle channel and 0% of the other channels. Because the gain has dropped in the middle channel, the received signal has dropped. And, as a consequence, the *SNR* has decreased, assuming that the noise power has not changed.

4.7.2 Impact of number of subbands M

Keeping the results of the previous section in mind, the impact of the number of subbands on the output of the beamformer is now investigated. In particular, the

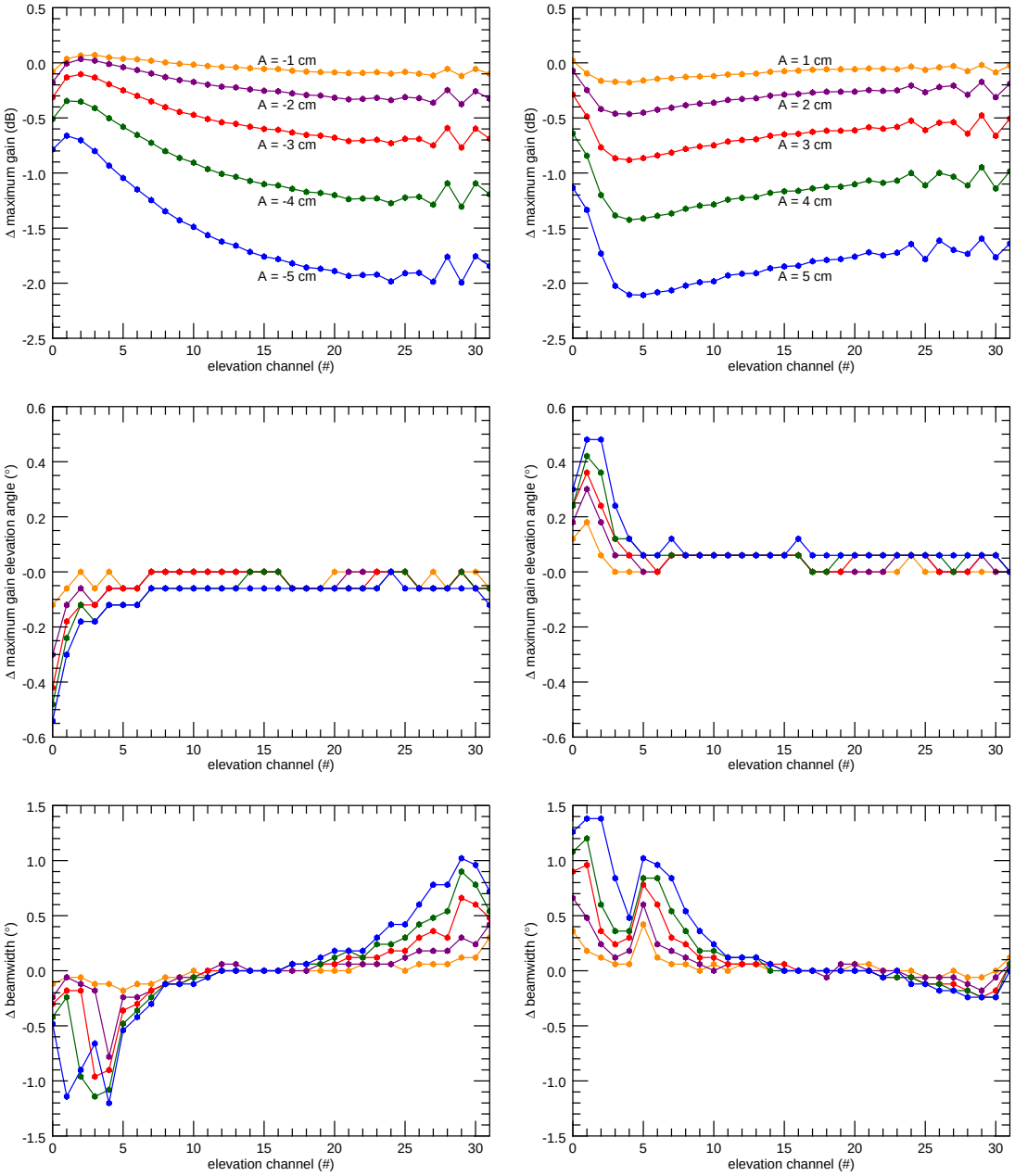

Figure 4.23: Deviation of antenna parameters. Top row: gain; middle row: maximum gain elevation; bottom row: beamwidth. Left column: $A = -1 \ldots -5$ cm. Right column: $A = 1 \ldots 5$ cm.

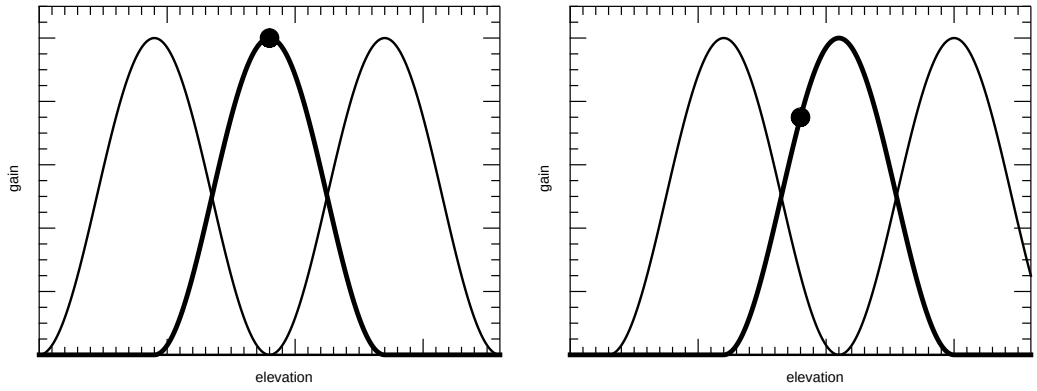

Figure 4.24: Antenna patterns of three elevation channels (left), and shifted in elevation (right).

case from section 4.4.2 with $A = 5$ cm is taken as the example, and compared to the parabolic reflector without deformation. In that case the impact of the deformation on gain, elevation where maximum gain occurs, and beamwidth is significant. In Fig. 4.25 the output of the beamformer is shown for $M = 1$, 2, 3, 5, 10, and 20. In all cases the number of filter coefficients is $N_{\text{coef}} = 201$, to ensure that all subbands are sufficiently filtered. In all plots a dashed line is used for the reflector without deformation, and a solid line is used for the deformed reflector.

In the top left corner of Fig. 4.25 ($M = 1$) very large differences are observed between the two cases. In the top right corner ($M = 2$) the differences between the subbands for the two cases are visible. But as the number of subbands increases the jumps between the subbands get smaller and smaller. For both cases, i.e., for the reflector without deformation and with deformation, the pulse is almost completely restored when M is large. The remaining difference between the two cases is the reduced output level for the deformed reflector, i.e., a drop in *SNR*.

4.7.3 Limited impact on *PSLR*, *ISLR*, and Δr

In all cases it was observed that the deformation of the reflector had little impact on the DBF parameters *PSLR*, *ISLR*, and Δr. Here, the investigation of section 4.7.2 is continued. For varying M, the four DBF parameters are computed for the reflector without deformation and the reflector with deformation. For each parameter the value of the case without deformation is subtracted from the value for the case with deformation. In Table 4.10 the differences in *SNR*, *PSLR*, *ISLR*, and Δr are shown for various M.

The difference in *SNR* rapidly converges to slightly more than 7 dB. The differences between the two cases for the other parameters rapidly converges to zero. In conclusion, the processing has removed the impact of the deformation on the *PSLR*, the *ISLR*, and the Δr. What remains is the impact on the *SNR*.

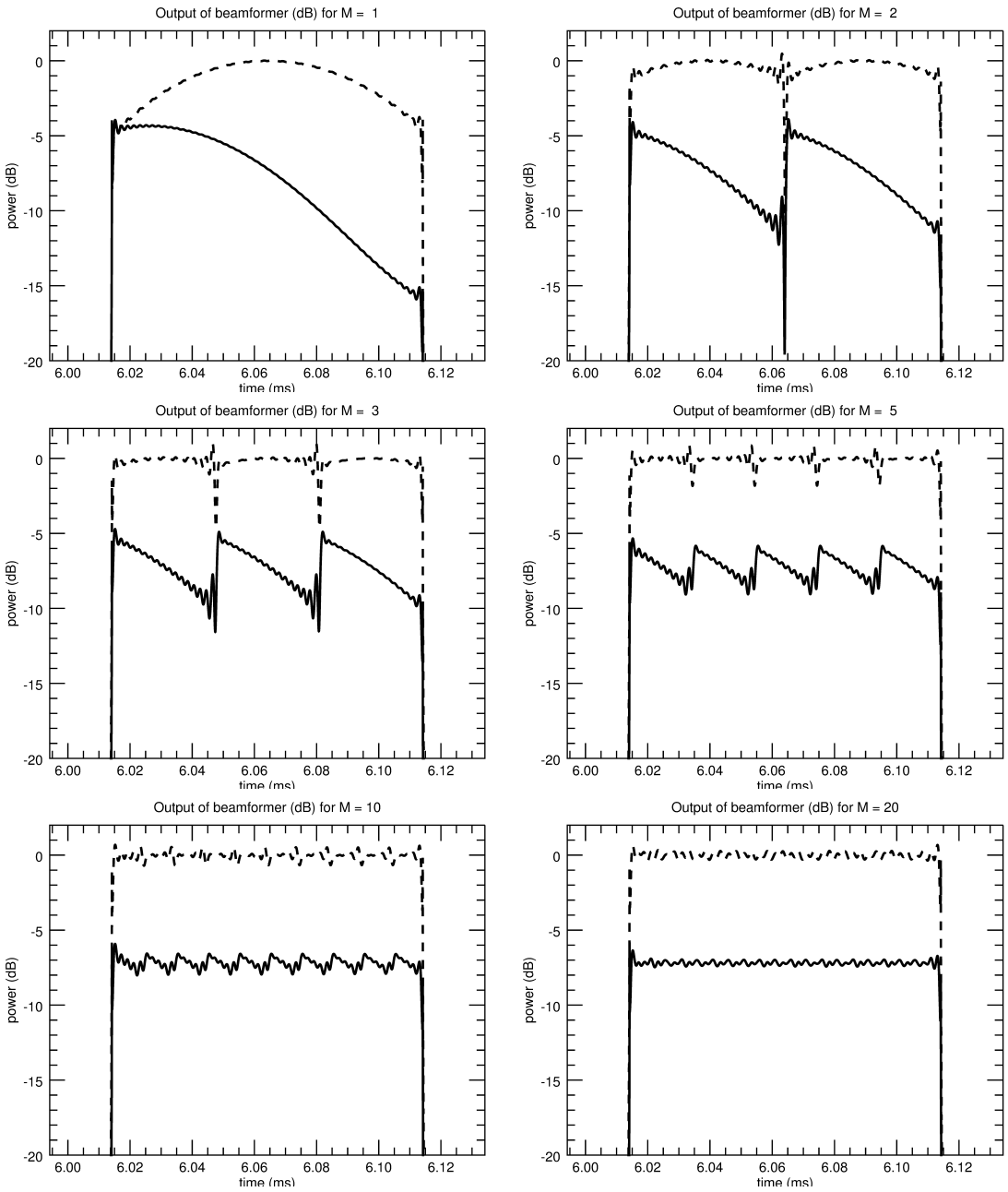

Figure 4.25: Output of beamformer for $M = 1$, 2, 3, 5, 10, and 20. Parabolic reflector: dashed line. Deformed reflector: solid line.

Table 4.10: Change in DBF parameters for various M.

M	1	2	3	4	5	10	20
Δ *SNR* (dB)	-5.69	-6.71	-6.97	-7.06	-7.11	-7.17	-7.18
Δ *PSLR* (dB)	2.61	0.87	0.31	0.17	0.11	0.03	0.00
Δ *ISLR* (dB)	3.41	1.09	0.88	0.70	0.56	0.20	0.05
Δ (Δr) (m)	0.06	0.32	0.00	0.00	0.00	0.00	0.00

4.8 Conclusions and recommendations

This chapter considered the impact of reflector deformations on antenna parameters, such as gain and beamwidth, and on DBF performance for a point target at boresight. The number of possible deformations is infinite. Here, a select set of deformations sinusoidal in radius and angle is considered, as well as deformations one could expect in an "umbrella" type of unfurlable antenna.

It is found that each distinct type of deformation has distinct impact on the antenna parameters. In general, the impact on DBF performance is most pronounced on the *SNR*, and the impact on the other DBF parameters is usually much less. The reason is that the use of multibeam SCORE DBF enables accurate reconstitution of the pulse. As explained in section 4.7.3, this, in turn, results in a relatively small impact on *PSLR*, *ISLR*, and Δr, at the expense of a reduced *SNR*.

The first recommendation is to extend the analysis to non-boresight point targets, range ambiguities, and DBF in azimuth. Such extension will further the understanding of the impact of reflection deformations on DBF and SAR imaging performance. The second recommendation is to acquire more information of the deformations that may occur in orbit. Vendors of unfurlable reflector antennas likely have reliable data of deformations measured on Earth, and they may have data or estimates of deformations that may occur in orbit.

Chapter 5

Impact of frequency dependent antenna performance

In the previous chapters, it is assumed that the bandwidth B of the chirp is so low that frequency dependencies in the reflector antenna can be ignored. That is, to determine the baseband signal, in Eq. (2.2) the chirp is multiplied with the gain of the antenna at the center frequency. In reality, however, the gain of the antenna is frequency dependent. This can be viewed as the antenna acting as a frequency dependent filter for the chirp signal. For example, low frequency components of the chirp come out differently in receive mode compared to high frequency components due to the frequency dependent gain of the antenna. The question then is what the impact is on DBF performance of the chirp bandwidth and the frequency dependent behavior of the antenna. In this chapter the impact of the frequency dependent behavior of the antenna on the following three antenna parameters is investigated: antenna gain, elevation where maximum gain occurs, and beamwidth. And the impact on the following DBF parameters is considered: *SNR*, *PSLR*, *ISLR*, and slant range resolution Δr.

The analysis is first applied to the offset fed reflector antenna, which is also considered in the previous two chapters. The analysis is then extended to the case of a center fed reflector antenna. Before considering these two cases, the approach to incorporate the frequency dependency of the reflector in the computations is discussed first. Conclusions and recommendations are provided at the end of the chapter.

5.1 Calculating the received baseband signal

To include the frequency dependent behavior of the antenna, the computational burden in the model increases significantly. The burden increases when computing the received baseband signal, the weights required in SCORE DBF using MVDR, and when performing frequency adaptive beamforming. This increase in computational burden is discussed below in more detail.

Firstly, instead of simulating the reflector in GRASP at one frequency, a series of

simulations versus frequency must be undertaken. Note that the simulations must go beyond the 85 MHz bandwidth from 1215-1300 MHz. The reason is that frequency interpolation is required, and for interpolation at the edges of the bandwidth, i.e., at 1215 MHz and at 1300 MHz, additional frequency points are needed below and above the two edges, respectively. Exporting the GRASP patterns into the IDL environment requires building of a three dimensional complex array containing the radiation patterns. The three dimensions are: elevation channel, elevation angle, and frequency.

Secondly, when computing the antenna pattern for a certain desired look angle required for SCORE DBF, a two-dimensional interpolation must be performed in elevation and frequency. Such an interpolation can be computationally very costly, especially if the interpolation kernels have to be large. To compute the received signal a convolution of the linear chirp with the frequency dependent antenna behavior must be performed. Implementing this is easy, computing it out is still somewhat of a burden for the following reason. Each time instant is associated with a chirp frequency and with a complex chirp signal. Thus, to compute the received signal, for each time instant the associated complex chirp signal is multiplied with the antenna pattern at the frequency that is associated with that particular time instant. And this operation is performed for all elevation channels.

Thirdly, when performing frequency adaptive beamforming, the MVDR beamforming weights must be computed for each of the center frequencies of the digital beams. For example, if the pulse is tracked with $M = 5$ beams, then the weights must be computed for 1223.5 MHz, 1240.5 MHz, 1257.5 MHz, 1274.5 MHz, and 1291.5 MHz. All the weights must be computed for each sample time and each of them requires interpolation of the antenna pattern in elevation and for the required frequency. This burden can be somewhat reduced by computing the antenna patterns precisely at the required frequencies first, which eliminates the need for interpolation over frequency.

5.2 Antenna with offset feeding

Tandem-L will use an offset array-fed reflector antenna to reduce EM interaction between the feed and the reflector. Besides possible frequency dependent EM interaction between reflector and feed, it is also expected that gain will increase with frequency. In GRASP the antenna is simulated from 1150 MHz to 1350 MHz in increments of 1 MHz. The need for such small increment will become apparent soon. In Fig. 5.1 the change in gain for five frequencies is shown as compared to the center frequency of 1257.5 MHz.

The figure shows that the gain of the boresight channels increases by approximately 0.9 dB per 100 MHz. The change in gain for channels with larger look angles, i.e., channels lower than 15, is much smaller. The change in beamwidth and the elevation angle where the maximum gain occurs are shown in Fig. 5.2 for the five frequencies and the 32 channels.

The figure shows relatively small changes in beamwidth and the elevation where

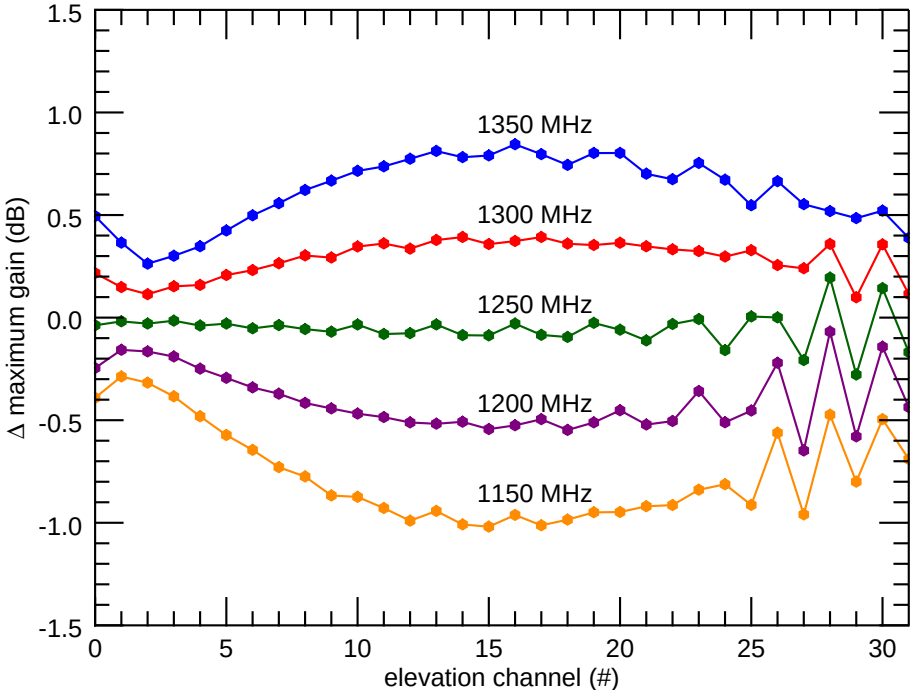

Figure 5.1: Change in antenna gain for five frequencies compared with the center frequency of 1257.5 MHz.

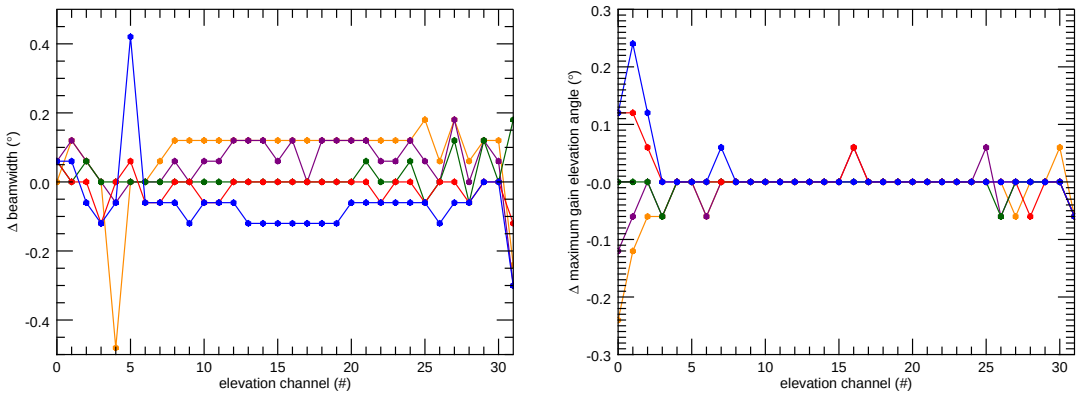

Figure 5.2: Change of beamwidth (left) and elevation where maximum gain occurs (right) for five frequencies (1150, 1200, 1250, 1300, 1350 MHz) w.r.t. the center frequency of 1257.5 MHz.

the maximum gain occurs. In Fig. 5.3 the gain and phase versus frequency are shown for channel 15 on the left and right, respectively. The gain shows an average increase of 0.9 dB per 100 MHz as well as a small ripple, believed to be due to the EM interaction between reflector and offset feed. The phase, shown on the right in Fig. 5.3, changes rapidly with frequency, cycling seven times through 360° between 1182 MHz and 1338 MHz, i.e., 360° every 22.3 MHz. The wavelength associated

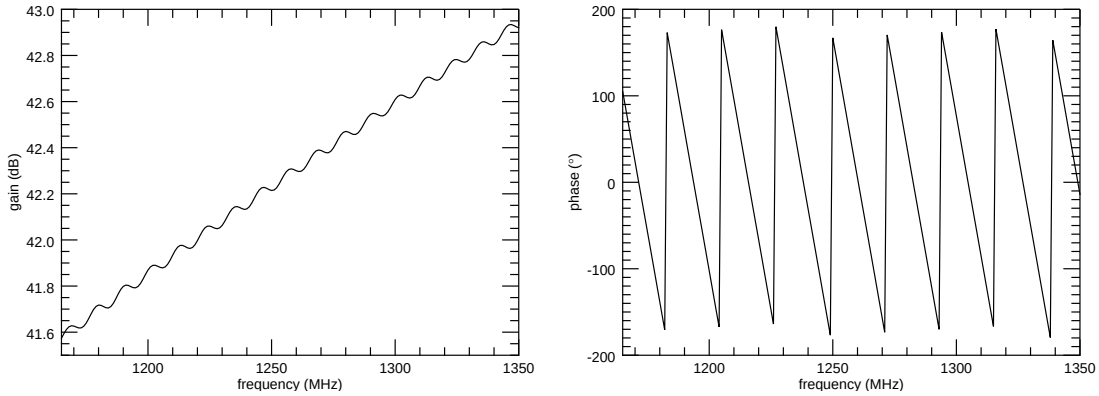

Figure 5.3: Gain and phase versus frequency for elevation channel 15.

with 22.3 MHz is 13.5 m, which is the focal length of the antenna. During the research no good explanation was found for this phase behavior. However, it was the reason for selecting a 1 MHz increment in the GRASP antenna simulations. These simulations started with much larger frequency increments, but it was found that the phase behavior was not captured appropriately and, subsequently, the frequency increments were reduced to 5 MHz and then to 1 MHz. In the DBF calculations that follow, the phase of the far field results was set to zero.

To investigate the impact of the frequency dependent antenna behavior, the following three cases are considered.

1. Case I: The baseline case, in which the antenna behavior is assumed frequency independent, i.e., the received signal and the SCORE MVDR weighting coefficients are computed based on the antenna performance at the center frequency of 1257.5 MHz.

2. Case II: The antenna behavior is assumed frequency dependent when computing the received signal. However, for computing the SCORE MVDR weighting coefficients only the antenna behavior at the center frequency is used.

3. Case III: The received signal and the SCORE MVDR weighting coefficients are computed based on the frequency dependent behavior of the antenna. In the following, this is referred to as frequency adaptive DBF.

For all three cases the DBF parameters (*SNR*, *PSLR*, *ISLR*, and Δr) are computed for $M = 1$, 2, 3, 4, 5, and 10, and $N_{\text{coef}} = 1$, 5, 11, 21, 51, and 101. In Table 5.1 the three cases are compared for $M = 10$, $N_{\text{coef}} = 21$. These results are very similar for other settings of M and N_{coef}. When comparing Case II with Case I, and Case III with Case II, only very small changes in the four DBF parameters are observed.

5.3 Antenna with center feeding

The analysis of the previous section is repeated with the feed-array placed in the center, instead of at an offset. The antenna is simulated in GRASP between 1150

Table 5.1: Change in DBF parameters for offset feeding ($M = 10$, $N_{\text{coef}} = 21$).

	Δ *SNR* (dB)	Δ *PSLR* (dB)	Δ *ISLR* (dB)	Δ (Δ r) (m)
Case II - Case I	-0.005	-0.007	-0.006	0.000
Case III - Case II	-0.003	0.009	0.006	0.000

MHz and 1350 MHz in 1 MHz increments. In Fig. 5.4 on the left, the antenna gain is shown for 1150, 1200, 1250, 1300, and 1350 MHz. In the same figure on the right the change in antenna gain w.r.t. the gain at the center frequency of 1257.5 MHz is shown.

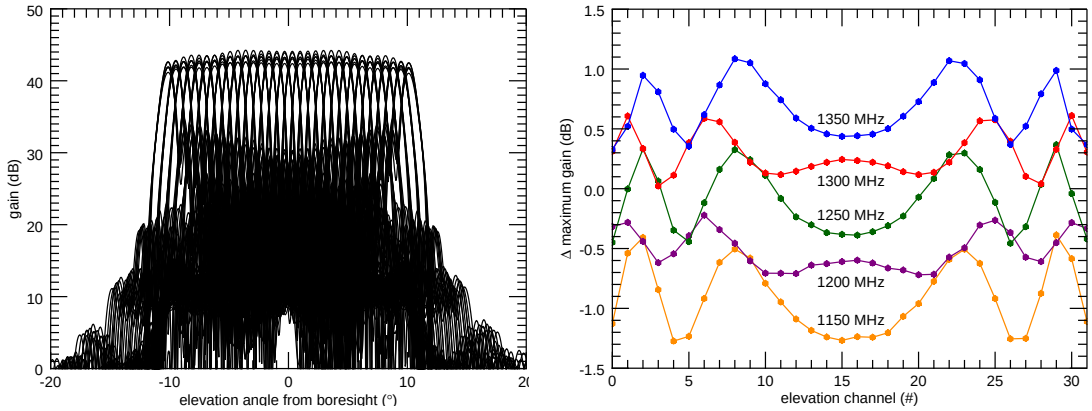

Figure 5.4: Antenna gain (left) and change in antenna gain compared with the center frequency of 1257.5 MHz(right) for five frequencies.

In Fig. 5.5 the change in gain (left) and the change in elevation angle of maximum gain (right) are shown w.r.t. the center frequency for the five aforementioned frequencies.

From Fig. 5.4 and Fig. 5.5 it is concluded that the gain fluctuates about 2 dB in the frequency range of 1150-1350 MHz, and that the beamwidth and the elevation where maximum gain occurs remain stable.

To investigate the antenna performance further, in Fig. 5.6 the gain and phase versus frequency for channel 15 are shown on the left and right, respectively.

The general trend of an increase in gain with frequency is observed again. Also, the oscillatory fluctuations in the gain have increased in magnitude as compared to the offset case shown in Fig. 5.3 on the left. As before, the phase changes rapidly with frequency. Because at the time of the research there was no good explanation for this phase behavior, the phase was reset to zero for all frequencies and all channels.

To investigate the impact of the frequency dependent antenna behavior, the three cases, discussed in the previous section, are considered again. For all three cases the DBF parameters (*SNR*, *PSLR*, *ISLR*, and Δr) are computed for $M = 1, 2, 3,$

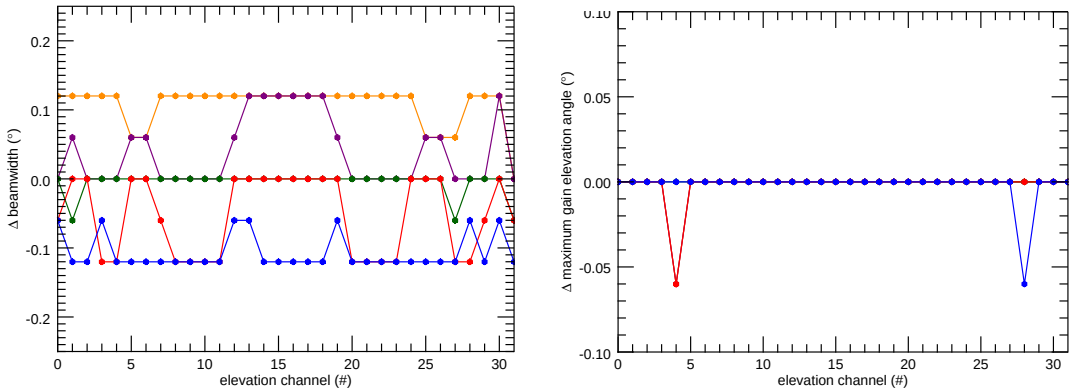

Figure 5.5: Change of beamwidth (left) and elevation where maximum gain occurs (right) for five frequencies (1150, 1200, 1250, 1300, 1350 MHz) w.r.t. the center frequency of 1257.5 MHz.

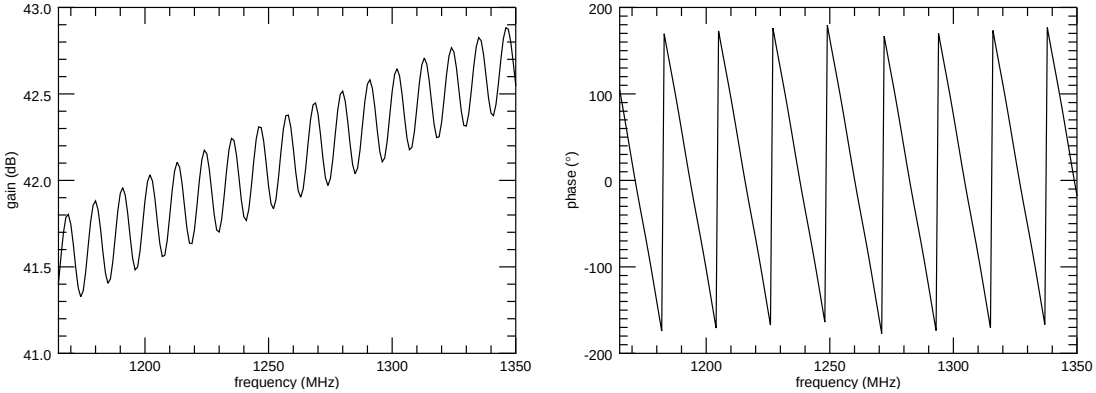

Figure 5.6: Gain and phase versus frequency for elevation channel 15.

4, 5, and 10, and $N_{\text{coef}} = 1$, 5, 11, 21, 51, and 101. In Table 5.2 the three cases are compared for $M = 10$, $N_{\text{coef}} = 21$. These results are very similar for other settings of M and N_{coef}.

Table 5.2: Change in DBF parameters for center feeding ($M = 10$, $N_{\text{coef}} = 21$).

	Δ *SNR* (dB)	Δ *PSLR* (dB)	Δ *ISLR* (dB)	Δ (Δ r) (m)
Case II - Case I	-0.263	0.006	0.020	0.000
Case III - Case II	0.004	-0.062	0.184	-0.007

Similar to the findings in the previous section, when comparing Case II with Case I, and case III with Case II, only very small changes in the four DBF parameters are observed.

5.4 Conclusions and recommendations

The impact on DBF performance of the frequency dependent antenna behavior is explored in this chapter for offset feeding and center feeding of the reflector. Three cases are considered: the baseline case, non-frequency adaptive DBF, and frequency adaptive DBF. As discussed in detail in section 5.1, the computational burden increases rapidly when considering the frequency dependent behavior. Not only must the antenna be analyzed in GRASP for many frequencies, two-dimensional interpolation over frequency and elevation may be required as well.

It is found that both in offset feeding and center feeding, the gain increases with frequency and also exhibits oscillatory fluctuations. An important finding is that the impact on the DBF parameters of the frequency dependent behavior is relatively small.

It is found that the phase of the antennas changes rapidly with frequency. At the time this research was performed, no good explanation was found for this phase behavior. In subsequent research at DLR by Dr.-Ing. Huber, it was found that a quasi phase center is located at the center of the reflector. Since in GRASP the phase reference is at the center of the global coordinate system, the additional length of 13.5 m is introduced as well as its associated phase behavior. Therefore, setting the phase equal to zero in sections 5.2 and 5.3 was reasonably justified, in retrospect.

The first recommendation of this chapter is to further investigate the phase behavior in the far field of the antennas as function of frequency. The second recommendation is to validate the GRASP results with more rigorous EM simulations. The interaction between feed and reflector impacts the performance of the antenna, as observed in the gain of channel 15 for the case of center feeding. GRASP incorporates such interactions in an approximate manner, and a rigorous EM analysis will help to improve confidence in the results further. The results indicate a relatively small impact of the frequency dependent behavior on the DBF performance for a point target at boresight. The final recommendation is to further extend the analysis to non-boresight point targets, range ambiguities, and DBF in azimuth.

Chapter 6

Conclusions and recommendations

Tandem-L aims to bring a SAR instrument in space employing an array-fed reflector antenna combined with DBF capability. This thesis investigates the impact of deformations in the reflector on some of the antenna parameters and some of the DBF parameters. Chapter 2 introduces the model used to develop the program in IDL. This model is then applied to the case of a reflector free of deformations in chapter 3 to generate baseline results. In chapter 4 the impact of various types of deformations is assessed and compared with the baseline results. Chapter 5 then considers the impact of frequency on the the antenna performance and on the DBF performance.

6.1 Conclusions

The first objective of this work is to assess the impact of reflector deformations on antenna performance and on DBF performance in elevation for a point target at boresight. The results, presented in chapter 4, show that deformations in the reflector can result in gain changes as well as the elevation where the maximum gain occurs. Further to that, the complete far field radiation pattern can be significantly affected, as shown in the example of Fig. 4.3. The impact of reflector deformations is most pronounced on the *SNR*, and is negligible on the *PSLR*, *ISLR*, and Δr when a sufficient number of subbands is used. As shown in the discussion in sections 4.7.2 and 4.7.3, by increasing the number of subbands M, the pulse is increasingly better reconstructed. And, therefore, the impact on the *PSLR*, *ISLR*, and Δr is decreased at the expense of an decreased *SNR*.

The second objective of this work is to assess the impact of the frequency dependent behavior of the antenna on antenna parameters and on DBF performance for offset feeding and center feeding. In case of offset feeding, an increase in gain of approximately 1.8 dB from 1150 MHz to 1350 MHz is observed for the channels around boresight, and smaller gain increases for the other elevation channels. In case of center feeding, a general increase in gain similar to offset feeding is observed, as well as significant gain fluctuations with frequency due to EM interaction between reflector and feed. The impact on DBF parameters is relatively small in both offset feeding and center feeding.

6.2 Recommendations

In section 3.4 the baseline case, used throughout this thesis, of a single point scatterer at boresight is discussed. In section 2.2, and also in Fig. 2.2, it is shown that the pulse does not travel with constant speed along the surface of Earth. The associated look angle increases initially very fast with time and the rate change of the look angle decreases as time progresses, as illustrated in Fig. 2.5. The DBF results will depend on the location of the point scatterer and, therefore, it is highly recommended to also do the analysis of chapter 3 and chapter 4 for point targets closer to nadir and also further away. For example, one can define five test cases: two at the extremes of the elevation scan, one at boresight, and two in between.

This thesis only considers the impact of reflector deformation on DBF in elevation. It is highly recommended that the analysis is expanded to DBF in range ambiguities, DBF in azimuth, and to SAR imaging. Developing a computational model in which impact of reflector deformations, and possibly other antenna imperfections, on SAR imaging quality can be analyzed, will be very useful to assess system performance and to specify system requirements. Further to that, such a model may also help to understand and mitigate problems that may occur once Tandem-L is launched.

The impact of reflector deformations is investigated in chapter 4. Deformations can be due to, for example, the sunlit-darkness cycles the satellite experiences and long term drift. In public literature not much information was found about actual deformations that may occur. It will be very useful to repeat the analysis for deformations which are informed by actual measurements of deformations on the ground and, perhaps, in orbit. Very likely, manufacturers of reflectors already have reliable data of deformations on the ground. Although this data may not entirely reflect the deformations that occur in orbit, it can still serve in benchmarking instrument performance under non-ideal circumstances.

In the IDL implementation of the model described in chapter 2, all signals are computed using the accuracy and floating point operation provided by IDL [7]. For example, the baseband signals are sampled with this accuracy and DBF weights are also computed with this accuracy. The accuracy of the actual hardware realization in Tandem-L may be different from what is used in the model. Therefore, it is recommended to make an analysis of the impact of reduced accuracy of sampling, data storage, and processing on the quality of SAR imaging in Tandem-L.

The basis for the analysis are GRASP simulations of the array-fed reflector antenna. GRASP uses the Physical Optics approximation to compute the EM performance of the antenna. There are no indications that there are any issues with this approach for the case analyzed here. Nevertheless, it is recommended that the antenna patterns are computed using another method as well, to validate the GRASP analysis. For example, TICRA has a Method of Moments (MoM) add-on to GRASP which may be able to perform a rigorous EM simulation of the antenna. In addition, the

deformations analyzed in this thesis are in the order of centimeters. This choice was a first cut to assess and understand the impact of deformations. The limited literature that was found on reflector deformations indicates that sub-millimeter deformations may occur, i.e., actual deformations are smaller than assumed here [8]. It will be useful if GRASP is also validated for such small deformations through simulations with other software and, possibly, measurements.

As discussed in section 2.5, MVDR beamforming is used in this thesis. MVDR beamforming requires knowledge of the noise covariance matrix between channels. In the absence of this knowledge, this matrix was assumed an identity matrix multiplied with the noise variance. This assumption essentially eliminates the impact of the noise covariance from the MVDR beamforming, which may be unrealistic. Therefore, it is recommended to incorporate realistic assessments of the noise covariance in the MVDR beamforming to assess its impact on DBF and imaging.

The SCORE temporal DBF is a key asset to Tandem-L. Various techniques and algorithms can be used for DBF. It is highly recommended to assess the various options in terms of performance and computational requirements. And, where needed, dedicated modifications can be made. For example, in this thesis MVDR beamforming using 32 elevation channels is considered. For any given digital beam, only a few channels contribute most of the energy. Therefore, it may make sense to modify the MVDR beamforming to use only, say, five channels for any given digital beam and any given time instant. Of course, as the SCORE beam tracks the pulse, the actual set of activated channels will continuously change. With this strategy, the amount of sampling and associated computations may be reduced considerably.

In the analysis presented in this thesis, the far field patterns of the azimuth channels are assumed aligned with the flight direction and the elevation channels are assumed to be aligned perpendicular to it. In reality, small deviations may occur, which may distort high resolution SAR imaging. Therefore, it is recommended to incorporate possibility of such deviations in the model.

Bibliography

[1] G. Krieger, A. Moreira, M. Zink, I. Hajnsek, S. Huber, M. Villano, K. Papathanassiou, M. Younis, P. L. Dekker, M. Pardini, D. Schulze, M. Bachmann, D. B. Tridon, J. Reimann, B. Bräutigam, U. Steinbrecher, C. Tienda, M. S. Ferrer, M. Zonno, M. Eineder, F. D. Zan, A. Parizzi, T. Fritz, E. Diedrich, E. Maurer, R. Münzenmayer, B. Grafmüller, R. Wolters, F. te Hennepe, R. Ernst, and C. Bewick, "Tandem-L: Main results of the phase A feasibility study," in *Geoscience and Remote Sensing Symposium (IGARSS)*, 2016.

[2] S. Huber, M. Villano, M. Younis, G. Krieger, A. Moreira, B. Grafmüller, and R. Wolters, "Tandem-L: Design concepts for a next-generation spaceborne SAR system," in *11th European Conference on Synthetic Aperture Radar*, 2016.

[3] M. Bachmann, D. B. Tridon, F. D. Zan, G. Krieger, and M. Zink, "Tandem-L observation concept an acquisition scenario for the global scientific mapping machine," in *11th European Conference on Synthetic Aperture Radar*, 2016.

[4] HARRIS, "IDL software - data visualization software." `http://www.harrisgeospatial.com/ProductsandTechnology/Software/IDL.aspx`, 2017.

[5] S. Huber, *Spaceborne SAR Systems with Digital Beamforming and Reflector Antenna*. PhD thesis, 2014. `http://elib.dlr.de/76420/1/Dissertation_Huber.pdf`.

[6] TICRA, "GRASP." `http://www.ticra.com/products/software/grasp`, 2017.

[7] HARRIS, "Accuracy and floating point operations." `https://www.harrisgeospatial.com/docs/accuracy_and_floating_po.html`, 2017.

[8] L. Datashvili, H. Baier, E. Wehrle, T. Kuhn, and J. Hoffmann, "Large shell-membrane space reflectors," in *51st AIAA/ASME/ASCE/AHS/ASC Structures, Structural Dynamics, and Materials Conference*, 2010.